

# Exploring the Computational Feasibility of Direct Pseudoinversion of the Encoding Matrix for MR Image Reconstruction (Pinv-Recon)

Kylie Yeung<sup>1,2,3</sup>, Christine Tobler<sup>4</sup>, Rolf F Schulte<sup>5</sup>, Benjamin White<sup>1</sup>, Anthony McIntyre<sup>3</sup>, Sébastien Serres<sup>6,7</sup>, Peter Morris<sup>8</sup>, Dorothee Auer<sup>8,9,10</sup>, Fergus V Gleeson<sup>2,3</sup>, Damian J Tyler<sup>1,11,+</sup>, James T Grist<sup>1,3,+,\*</sup>, and Florian Wiesinger<sup>5,12,+</sup>

<sup>1</sup>Oxford Centre for Clinical Magnetic Resonance (OCMR), University of Oxford, Oxford, OX3 9DU, United Kingdom

<sup>2</sup>Department of Oncology, University of Oxford, Oxford, OX3 7DQ, United Kingdom

<sup>3</sup>Department of Radiology, Oxford University Hospitals NHS Trust, Oxford, OX3 7LE, United Kingdom

<sup>4</sup>MATLAB, The Mathworks, Munich, 81673, Germany

<sup>5</sup>GE HealthCare, Munich, 80807, Germany

<sup>6</sup>School of Life Sciences, University of Nottingham, Nottingham, NG7 2TQ, United Kingdom

<sup>7</sup>The David Greenfield Human Physiology Unit, University of Nottingham, Nottingham, NG7 2UH, United Kingdom

<sup>8</sup>Sir Peter Mansfield Imaging Centre, University of Nottingham, Nottingham, NG7 2QX, United Kingdom

<sup>9</sup>Mental Health and Clinical Neuroscience, School of Medicine, University of Nottingham, Nottingham, NG7 2TU, United Kingdom

<sup>10</sup>NIHR Nottingham Biomedical Research Centre/Nottingham Clinical Research Facilities, QMC, Nottingham, NG7 2UH, United Kingdom

<sup>11</sup>Department of Physiology, Anatomy and Genetics, University of Oxford, Oxford, OX1 3PT, United Kingdom

<sup>12</sup>Department of Neuroimaging, Institute of Psychiatry, Psychology & Neuroscience, King's College London, London, SE5 8AF, United Kingdom

\*Corresponding author: james.grist@cardiov.ox.ac.uk

<sup>+</sup>These authors contributed equally to this work.

May 5, 2025

This is a preprint of a submission to *Scientific Reports*.

## Abstract

Image reconstruction in Magnetic Resonance Imaging (MRI) is fundamentally a linear inverse problem, such that the image can be recovered via explicit pseudoinversion of the encoding matrix by solving  $\mathbf{data} = \mathbf{Encode} \times \mathbf{image}$  — a method referred to here as Pinv-Recon. While the benefits of this approach were acknowledged in early studies, the field has historically favored fast Fourier transforms (FFT) and iterative techniques due to perceived computational limitations of the pseudoinversion approach. This work revisits Pinv-Recon in the context of modern hardware, software, and optimized linear algebra routines. We compare various matrix inversion strategies, assess regularization effects, and demonstrate incorporation of advanced encoding physics into a unified reconstruction framework.

While hardware advances have already significantly reduced computation time compared to earlier studies, our work further demonstrates that leveraging Cholesky decomposition and block-wise inversion leads to a two-order-of-magnitude improvement in computational efficiency over previous Singular Value Decomposition-based implementations. Moreover, we demonstrate the versatility of Pinv-Recon on diverse *in vivo* datasets encompassing a range of encoding schemes, starting with low- to medium-resolution functional and metabolic imaging and extending to high-resolution cases. Our findings establish Pinv-Recon as a practical and adaptable reconstruction method that aligns with the increasing emphasis on open-source and reproducible MRI research.

**Keywords:** Pinv-Recon, MRI, image reconstruction, SENSE reconstruction, regularization

## 1 Introduction

Magnetic resonance imaging (MRI) is a cornerstone of modern medical diagnostics, providing unparalleled soft tissue contrast and functional information. Its widespread adoption, with over 100 million scans performed annually [1], demonstrates its clinical importance. Central to the effectiveness of MRI is the process of image reconstruction [2, 3], which converts the raw k-space data into diagnostic images. MRI reconstruction has traditionally relied on the fast Fourier transform (FFT) to rapidly transform uniformly sampled Cartesian k-space data into images. However, FFT-based methods struggle with non-Cartesian sampling patterns, parallel imaging (multi-coil data), and other complex encoding schemes, necessitating more sophisticated reconstruction algorithms [4, 5, 6]. As a result, iterative reconstruction techniques and other advanced methods have been developed to address these challenges, improving image quality while managing computational complexity.

From a mathematical perspective, MR image reconstruction can be understood as a linear inverse problem, where the unknown image is encoded into the measured k-space data via an encoding matrix,  $\mathbf{Encode}$  [7]. Direct inversion of this encoding matrix, while theoretically possible, has historically been deemed computationally prohibitive in terms of both memory requirements and computational time, because the complexity scales on the order of  $N^3$ , where  $N$  is the number of elements on one side of  $\mathbf{Encode}$  [5, 8, 9, 10]. This is in contrast to the computational complexity of  $O(N \log N)$  of the FFT. Early attempts, for example Van de Walle *et al.* in 2000 [11], explored pseudoinverse-based reconstruction but were constrained by the computing resources of that era. Pruessmann’s seminal 2001 paper on sensitivity encoding with arbitrary k-space trajectories also illustrated the challenges of direct matrix inversion on early-2000s hardware and advocated for more efficient iterative solutions [7]. Since then, few studies have revisited the computational burden of direct matrix inversion in MRI.

Recent advances in computational hardware and software have significantly altered the landscape of numerical linear algebra computations. The transition to 64-bit operating systems in the early 2000s enabled the handling of very large arrays (exceeding the 4 GB memory limit of 32-bit systems) [12], and compatible software packages have emerged in the subsequent years. The rise of artificial intelligence and deep learning has driven rapid advancements in multi-threaded central processing units (CPUs), parallel computing platforms, powerful graphical processing units (GPUs), and tensor processing units (TPUs). Combined with highly optimized numerical linear algebra libraries, these developments have made large-scale matrix operations, such as direct pseudoinversion of the encoding matrix, increasingly practical for MR image reconstruction in the current clinical environment.

In this work, we investigate the computational feasibility and potential advantages of direct pseudoinversion of the encoding matrix for MR image reconstruction, an approach we term ‘Pinv-Recon’. By leveraging modern computational resources, we demonstrate that Pinv-Recon can be a viable alternative to conventional reconstruction methods, especially for low- to medium-resolution imaging applications. This approach offers several benefits, including simplicity of implementation, inherently interpretable regularization, the ability to account for multiple intertwined encoding mechanisms and distortions in a single framework, and support for computing relevant image reconstruction metrics, such as the spatial response function (SRF) and the noise matrix.

The remainder of this paper is organized as follows. *Algebraic Background* covers potential matrix decomposition methods for directly computing the pseudoinverse of the encoding matrix for MR image reconstruction, expanding beyond the previously suggested method of singular value decomposition (SVD). *Computational Evaluation and Numerical Simulations* evaluates Pinv-Recon in terms of computational feasibility, the impact of different regularization approaches, and its versatility in incorporating various encoding mechanisms and distortions. *Exemplary Applications* include Pinv-Recon of a range of 2D and 3D imaging experiments, including hyperpolarized Carbon-13 brain, hyperpolarized Xenon-129 lung, proton knee, proton brain (the ISMRM CG-SENSE challenge dataset [13]), and proton abdominal imaging. The final section provides a discussion of the advantages, limitations, and potential future directions of Pinv-Recon.

## 2 Algebraic Background

Inspired by the notation introduced by Pruessmann *et al.* in *SENSE: Sensitivity Encoding for Fast MRI* [14], we first formalize the MR image reconstruction problem and then outline possible solutions, including various methods for pseudoinversion of the encoding matrix. MRI can be modeled as a linear forward mapping, or “encoding”, of the unknown image onto the raw k-space data, mediated by an encoding matrix, **Encode**:

$$\mathbf{data} = \mathbf{Encode} \times \mathbf{image}, \quad (1)$$

where both **data** and **image** have been flattened into 1D vectors. **Encode** is a dense complex matrix that relates each measured data point to all unknown image voxels. In its simplest form, **Encode** considers only basic gradient encoding (Fourier encoding) and reduces to a Fourier matrix, with each element written as:

$$\exp(j \cdot 2\pi \cdot \mathbf{k}_{i_k} \cdot \mathbf{r}_{i_r}) \quad (2)$$

where  $j = \sqrt{-1}$  is the imaginary unit,  $\mathbf{k}_{i_k}$  is the  $i_k$ th k-space sampling point, and  $\mathbf{r}_{i_r}$  is the  $i_r$ th spatial location (voxel position). The k-space points, and spatial locations, can both be discretized to any arbitrary grid, including Cartesian, non-Cartesian, uniform, non-uniform, overdiscretized, and masked ones (See Supplementary Material 1).

MRI reconstruction can be considered the inverse problem of this forward mapping, i.e., solving for the unknown **image** given the measured **data** and the known **Encode** matrix that encapsulates all the encoding physics and geometry. Image reconstruction can be performed by first explicitly inverting **Encode** to find the reconstruction matrix (**Recon**) and then applying it to the **data** by a single matrix-vector multiplication:

$$\mathbf{image} = \mathbf{Recon} \times \mathbf{data}, \quad \text{where } \mathbf{Recon} = \mathbf{Encode}^{-1}, \quad (3)$$

or by solving for the **image** implicitly without explicitly forming **Recon**, for example via iterative algorithms.

## 2.1 The Moore–Penrose Pseudoinverse and the Normal Equation

The true inverse of a matrix exists only if the matrix is square and of full rank. However, **Encode** is typically rectangular (total number of measurements  $N_k$  by total number of unknowns  $N_r$ ) in most MR applications. The Moore–Penrose pseudoinverse provides a generalized solution for inverting such rectangular matrices [15]. Using the normal equations, the pseudoinverse can be defined for two cases:

- **Overdetermined problems** ( $N_k > N_r$ ): where the left-pseudoinverse solution gives

$$\mathbf{Recon} = \mathbf{Encode}^{-1} = (\mathbf{Encode}^H \mathbf{Encode})^{-1} \mathbf{Encode}^H,$$

providing the least-squares solution for the image (i.e., minimizing  $\|\mathbf{Encode} \times \mathbf{image} - \mathbf{data}\|$ ), and

- **Underdetermined problems** ( $N_k < N_r$ ): where the right-pseudoinverse solution gives

$$\mathbf{Recon} = \mathbf{Encode}^{-1} = \mathbf{Encode}^H (\mathbf{Encode} \mathbf{Encode}^H)^{-1},$$

providing the minimum-norm solution (i.e.,  $\mathbf{image} = \arg \min_{\mathbf{image}} \|\mathbf{image}\|^2$  s.t.  $\mathbf{data} = \mathbf{Encode} \times \mathbf{image}$ ).

The two cases can be derived from one another by simple Hermitian transpose operations. In that sense, it is sufficient to consider only one of the two cases, and we focus on the more typical overdetermined problem for the remainder of this work.  $\mathbf{Encode}^H \mathbf{Encode}$  in Eq. 4, which is square and invertible (with regularization as needed), is also referred to as the Gram matrix.

The following sections highlight several commonly used matrix pseudoinversion methods and linear system solvers. Among these, only truncated SVD-based pseudoinversion and iterative solvers have been commonly considered in the context of MR reconstruction prior to this work [8, 9, 11, 16].



## 2.2 Direct Inversion Methods

Direct inversion methods decompose the rectangular encoding matrix directly, without explicitly forming the Gram matrix, to compute the pseudoinverse.

**Singular Value Decomposition:** The Singular Value Decomposition (SVD) [17] factorizes and inverts the encoding matrix as:

$$\begin{aligned}\mathbf{Encode} &= \mathbf{U} \Sigma \mathbf{V}^H, \\ \mathbf{Recon} &= \tilde{\mathbf{V}} \tilde{\Sigma}^{-1} \tilde{\mathbf{U}}^H,\end{aligned}\tag{4}$$

where  $\mathbf{U}$  and  $\mathbf{V}$  are unitary matrices (of dimensions  $N_k \times N_k$  and  $N_r \times N_r$ , respectively) and  $\Sigma$  is a diagonal matrix containing the singular values  $\sigma_i$  of  $\mathbf{Encode}$ . The set of singular values (the SVD spectrum) provides a useful visual impression of the overall conditioning of  $\mathbf{Encode}$ .  $\tilde{\mathbf{V}}, \tilde{\Sigma}, \tilde{\mathbf{U}}$  are the truncated versions of each matrix respectively. Truncated SVD (tSVD) regularizes and ensures stability in the inversion by removing small singular values. The ratio of the largest and the remaining smallest singular value in  $\tilde{\Sigma}$  is then referred to as the condition number ( $\kappa$ ). Typically, the truncation threshold is set to capture a predetermined percentage of the energy of the original data, such as 95%. Note that reconstruction matrices with different condition numbers can be realized from the same original untruncated SVD decomposition.

**QR Decomposition:** QR decomposition [18] factors a matrix into orthogonal and triangular factors and provides the pseudoinverse as:

$$\begin{aligned}\mathbf{Encode} &= \mathbf{Q} \mathbf{R}, \\ \mathbf{Recon} &= \mathbf{R}^{-1} \mathbf{Q}^H\end{aligned}\tag{5}$$

where  $\mathbf{Q}$  is an  $N_k \times N_r$  matrix with orthonormal columns and  $\mathbf{R}$  is an  $N_r \times N_r$  upper triangular matrix.  $\mathbf{Q}$  and  $\mathbf{R}$  may also be truncated for regularization. QR decomposition is typically faster than SVD and maintains good numerical stability, but does not provide the information of the SVD spectrum.

## 2.3 Normal-Equation-Based Methods

Normal-equation-based methods avoid directly inverting the raw rectangular  $\mathbf{Encode}$  matrix. Instead, they decompose the smaller square Gram matrix to derive the pseudoinverse, which is computationally more efficient than decomposing the full rectangular matrix. However, it can be problematic for ill-conditioned problems because the condition number of  $\mathbf{Encode}^H \mathbf{Encode}$  is squared compared to that of  $\mathbf{Encode}$ . This issue can be mitigated by applying appropriate Tikhonov regularization [19, 20], which improves the conditioning of the matrix, similar to singular value truncation. Additionally, Tikhonov regularization helps ensure positive-definiteness, a required property for certain matrix decomposition methods. It is implemented by adding a small  $\lambda^2$  to the diagonal of the Gram matrix:

$$\begin{aligned}\mathbf{Encode}^{-1} &= (\mathbf{Encode}^H \mathbf{Encode} + \lambda^2 \mathbf{I})^{-1} \mathbf{Encode}^H \\ \mathbf{image}_\lambda &= (\mathbf{Encode}^H \mathbf{Encode} + \lambda^2 \mathbf{I})^{-1} \mathbf{Encode}^H \mathbf{data}.\end{aligned}\tag{6}$$

For very large  $\lambda^2$ , this solution approaches a simple conjugate-phase reconstruction [21], whereas smaller  $\lambda^2$  values more fully account for density compensation and deapodization. The choice of  $\lambda^2$

can be guided by principles like Morozov’s discrepancy principle, which suggests selecting  $\lambda^2$  such that the residual  $\|\mathbf{Encode\_image}_\lambda - \mathbf{data}\|$  is on the order of the noise level in the data [22].

**Eigenvalue Decomposition:** Eigenvalue decomposition [17] applies to the Gram matrix and gives **Recon** using the normal equation:

$$\begin{aligned}\mathbf{Encode}^H \mathbf{Encode} + \lambda^2 \mathbf{I} &= \mathbf{P} \mathbf{\Lambda} \mathbf{P}^H, \\ \mathbf{Recon} &= \mathbf{P} \mathbf{\Lambda}^{-1} \mathbf{P}^H \mathbf{Encode}^H\end{aligned}\tag{7}$$

where the columns of  $\mathbf{P}$  are eigenvectors and  $\mathbf{\Lambda}$  is a diagonal matrix of eigenvalues. Note that  $\mathbf{P}^{-1} = \mathbf{P}^H$  for a symmetric Gram matrix. Eigenvalue decomposition is a special case of the SVD applied to a symmetric matrix, thus resulting in only one base  $\mathbf{P}$ . The eigenvalues of the Gram matrix are equivalent to the singular values of **Encode** squared. Regularization can be applied by truncating the eigenvalues, by adding  $\lambda^2$  to the eigenvalues for Tikhonov regularization, or by combining both.

**Cholesky Decomposition:** Cholesky decomposition [17] is known for being one of the most computationally efficient matrix decomposition algorithms, serving as an attractive choice for Pinv-Recon. It is a specialized method for square, symmetric positive definite matrices, factorizing the Gram matrix and giving **Recon** as:

$$\begin{aligned}\mathbf{Encode}^H \mathbf{Encode} + \lambda^2 \mathbf{I} &= \mathbf{L} \mathbf{L}^H, \\ \mathbf{Recon} &= (\mathbf{L}^{-1})^H \mathbf{L}^{-1} \mathbf{Encode}^H\end{aligned}\tag{8}$$

where  $\mathbf{L}$  is a lower triangular matrix. The inversion of  $\mathbf{L}$  is computationally efficient because of its triangular structure.

When faced with large encoding matrices that do not fit into computer or GPU memory, block matrix operations can be used to invert the matrix in a block-wise manner [17]: breaking down **Encode** or the Gram matrix into smaller blocks, inverting the smaller blocks, then recombining them. This linear algebra technique has not previously been applied to MR image reconstruction by direct pseudoinversion of the encoding matrix, but could enable better leveraging of available computational power and GPU acceleration.

## Direct Solution without explicit inversion

The matrix inversion methods described above explicitly calculate the pseudoinverse of **Encode** to obtain the reconstruction operator **Recon**, and we will refer to them collectively as Pinv-Recon. Other approaches exist which directly obtain **image** without calculating **Recon**, for example directly solving equation (1) with simple matrix division of **data** by **Encode**, adding Tikhonov regularization to ensure numerical stability.

Iterative algebraic reconstruction techniques, such as conjugate-gradient (CG) methods, may also utilize the explicit encoding matrix and solve for **image** without finding **Recon**, and have been widely explored due to their computational efficiency. For example, it has been explored by Kadam and Hu in 1998 [9], by Wilm *et al.* in 2011 [23], and by Li *et al.* in 2015 [24], incorporating various encoding mechanisms such as  $B_0$  distortion and coil sensitivity which will be further discussed in Section 3.3. We will hereafter refer to this approach as  $CG_{Encode}$ , to distinguish it from other iterative approaches which do not use the explicit encoding matrix.

## 2.4 Image Metrics Derived from Recon

**Recon**, which is generally not calculated in modern MR image reconstruction algorithms or in direct solution methods such as  $CG_{Encode}$ , contains useful information for the calculation of relevant image metrics [25, 26]. The spatial response function (SRF) measures the proportion of a pixel represented in the reconstructed image. It effectively calculates the forward encoding step followed by the backward projection, and accounts for the fact that each image value does not exclusively reflect the magnetization at the corresponding position, but also exhibits contamination from surrounding signals. Using **Recon** and **Encode**, the SRF matrix (**SRF**) of all image pixels can be calculated by simple matrix-matrix multiplication:

$$\mathbf{SRF} = \mathbf{Recon} \times \mathbf{Encode}. \quad (9)$$

In the optimal scenario, **SRF** approaches identity. An SRF map can be obtained by reshaping the diagonal elements of **SRF** to the image size, where a value of 1 indicates the signal from that pixel is fully represented in the final **image**. **Recon** also allows simple calculation of the noise matrix **X**, which reflects the noise propagated during reconstruction:

$$\mathbf{X} = \mathbf{Recon} \tilde{\Psi} \mathbf{Recon}^H \quad (10)$$

where  $\tilde{\Psi}$  is the noise covariance matrix.

## 3 Computational Evaluation and Numerical Simulations

### 3.1 Computational Time

Initial work was undertaken to explore the memory requirements and computation times for decomposing reconstruction matrices using different methods. Random complex single-precision matrices were generated to simulate encoding matrices for 2D image matrix sizes (MTX)  $32 \times 32$  up to  $320 \times 320$  (with equivalent MTX for 1D and 3D images noted in Table 1). Fig. 1a illustrates Pinv-Recon of the Shepp-Logan phantom for generic 1D, 2D and 3D sampling. The matrix decomposition times using SVD, QR, eigenvalue, and Cholesky decomposition in MATLAB (The Mathworks, MA, USA) were measured on a high-performance workstation (Intel® Xeon® Gold 6448 CPU,  $2 \times 32$  cores, 1 TB RAM; NVIDIA® A100 80 GB GPU), similar to those available on modern MR scanners. The results are summarized in Fig. 1b and 1c. Computational times required on a less powerful mobile workstation are also shown in Supplementary Material 2.

The computational time required for a  $\sim 2$  GB encoding matrix (approximately equivalent to a MTX  $128 \times 128$  2D image with full Fourier encoding) ranged from under a second to several minutes, depending on the inversion method used. Among the four methods, Cholesky decomposition was fastest, followed by eigenvalue decomposition, QR, and then SVD. This ranking is expected from their algorithmic cost. All methods exhibited scaling approximately proportional to the cube of the matrix dimension ( $O(N^3)$ ). Use of the GPU provided additional speedups for the larger matrices (roughly  $2 \times$  acceleration for matrices above 2 GB), though the benefit varied with the decomposition method and matrix size. A block-wise Cholesky algorithm was employed to invert matrices larger than the GPU memory (indicated by asterisks in Fig. 1c).

A few additional points are worth noting. For normal-equation-based approaches, an extra step of inverting the decomposed matrix and multiplying by **Encode**<sup>H</sup> may be required to form **Recon**

(c.f. Section 2.3), but the matrix decomposition itself dominates the runtime. The decomposition times for non-Cartesian trajectories (circular coverage of k-space) or masked images (spatial restriction to object coverage) will be shorter than images of equivalent MTX listed in Fig. 1c, which assume equal  $N_k$  and  $N_r$ , i.e. full Fourier encoding, for simplicity. For example, a MTX  $128 \times 128$  image sampled with 15776-point spiral, masked to a circular field-of-view (covering 86% of image space) results in an encoding matrix of only  $N_k \times N_r = 15776 \times 14090$ , and a Gram matrix of  $14090 \times 14090$ , requiring much shorter decomposition time than for  $N_k \times N_r = 16384 \times 16384$  ( $128^2 \times 128^2$ ). The present computational evaluation assumes single precision. If double precision (64-bit) were used instead, memory usage and computation time approximately double; conversely, emerging half-precision (16-bit) arithmetic could further accelerate these computations at the cost of reduced numerical stability.

### 3.2 Regularization

Regularization is an essential step in pseudoinverse reconstruction, determining the trade-off between noise amplification and resolution. We compared tSVD versus Tikhonov regularization using a Shepp–Logan phantom simulation. A MTX  $128 \times 128$  Shepp–Logan phantom was forward-encoded with an 8-arm spiral trajectory (Fig. 2a) and reconstructed using Pinv-Recon under varying noise and regularization settings. Shepp–Logan images of four different noise levels (0, 0.1, 1, and 10, with 0 corresponding to the noise-free case) were generated and forward encoded. TSVD reconstructions were performed while varying the energy cutoff (cumulative singular value energy from  $10^{-5}\%$  up to 100%), and Tikhonov reconstructions were performed while varying  $\lambda^2$  (from  $10^{-7}$  to  $10^5$  times the largest eigenvalue).

The log of the SVD spectrum (Fig. 2b) is shown, normalized to the maximum singular value. Truncation of the SVD at  $10^{-2}$  and  $10^{-4}$  is highlighted with the vertical gray grid lines. The square root of the singular values of  $\mathbf{Encode}^H \mathbf{Encode}$  after Tikhonov Regularization at corresponding values are plotted in black dotted lines. Fig. 2c and 2e show reconstructions using SVD truncation and Tikhonov regularization, respectively, with increasing noise levels (top to bottom) and decreasing regularization (left to right). Fig. 2d and 2f display mean squared errors (MSE) for different noise levels. The y-axis markers highlight convergence points:  $MSE_0$  (error between the Shepp–Logan image and a zero image) and  $\Delta Res$  (error between the Shepp–Logan image and an ‘ideal’ reference Shepp–Logan image accounting for the circular k-space field of view).

Insufficient regularization amplifies noise, particularly in low-noise scenarios, where minimal truncation suffices for a low MSE. As noise increases, stronger regularization is needed to prevent divergence from the reference image. However, excessive truncation degrades resolution, causing higher MSEs. In SVD truncation, only low-resolution components remain, resulting in a blurry image (Fig. 2c, left). Over-regularizing with Tikhonov regularization (large  $\lambda^2$ ) results in conjugate phase reconstruction, where the reconstructed image converges to a zero image (Fig. 2e, left).

In intermediate regimes, both regularization methods converged to similar reconstruction errors, and all matrix decomposition methods yielded virtually identical results when using the same Tikhonov regularization  $\lambda^2$ . The normalized MSEs between them are on the order of  $10^{-8}$ , indicating that the choice of regularization outweighs the choice of decomposition in terms of image reconstruction variability.

### 3.3 Generalized Encoding

We demonstrated the versatility of Pinv-Recon using a numerical Shepp–Logan phantom by incorporating multiple encoding components into **Encode**. Ideally, **Encode** can account for all relevant desired encoding mechanisms as well as undesired encoding distortions.

**Desired encoding mechanisms** include spatial localization via Fourier encoding (used in the majority of MR imaging), which can be complemented by advanced techniques such as parallel imaging to exploit spatially varying coil sensitivity profiles, and spectral encoding methods like Dixon’s chemical shift encoding using multiple echo times [25, 27]. These can be mathematically represented as individual factors in the encoding matrix. For example,

- **Coil sensitivity encoding:**

$$\mathbf{CoilSensitivity}_{i_{Rx}}(\mathbf{r}_{i_r})$$

where  $\mathbf{CoilSensitivity}_{i_{Rx}}$  is the spatial sensitivity profile of the  $i_{Rx}$ th receive coil, and

- **Multi-echo chemical shift encoding:**

$$\exp(j \cdot \Delta\mathbf{CS}_{i_{CS}} \cdot \mathbf{TE}_{i_{TE}})$$

where  $\Delta\mathbf{CS}_{i_{CS}}$  is the chemical shift frequency of the  $i_{CS}$ th species (with  $\mathbf{TE}_{i_{TE}}$  the  $i_{TE}$ th echo time).

**Undesired encoding distortions** inevitably occur in addition to these intended encoding mechanisms, and should be accounted for. Common distortions include:

- $B_0$  **off-resonance:**

$$\exp(j \cdot \Delta\mathbf{B0}_{i_r} \cdot t_{i_k})$$

where  $\Delta\mathbf{B0}_{i_r}$  is the local field inhomogeneity at voxel  $i_r$ , and  $t_{i_k}$  is the time of the  $i_k$ th readout [28],

- **Spatiotemporal gradient imperfections:**

$$\mathbf{k}_{i_k} \rightarrow \mathbf{k}'_{(i_k, i_r)}$$

where the true k-space location replaces the nominal k-space coordinate [29, 30, 31, 32], and

- **Spatial translation and rotation/Rigid-body motion:**

$$\mathbf{r}_{(i_r, i_k)} \rightarrow \mathbf{Rot}(t_{i_k}) \mathbf{r}_{i_r} + \Delta\mathbf{r}(t_{i_k}),$$

where  $\mathbf{Rot}(t_{i_k})$  is a rotation matrix and  $\Delta\mathbf{r}(t_{i_k})$  is a translation vector describing the motion (e.g. due to patient movement) at time  $t_{i_k}$ . This simplifies to a constant rigid-body shift if the imaging volume is not centered at the gradient isocenter but does not move during imaging.

Each of these factors can be incorporated as a multiplicative term modifying the encoding matrix or as a replacement for nominal k-space or image space coordinates. These encoding components can multiply together to form the net encoding relationship without breaking the linear mapping between **image** and **data**, allowing Pinv-Recon to solve for all these effects in one system.

Fig. 3 demonstrates incrementally including all of the above mechanisms and distortions, with the encoding matrix in the final column being:

$$\mathbf{Encode}_{(i_k, i_{\text{Rx}}, i_{\text{TE}}), (i_r, i_{\text{CS}})} = \underbrace{\exp(j 2\pi \mathbf{k}'_{(i_k, i_r)} \cdot (\mathbf{r}_{i_r} + \Delta \mathbf{r}))}_{\text{Gradient}} \times \underbrace{\mathbf{CoilSensitivity}_{i_{\text{Rx}}}(\mathbf{r}_{i_r} + \Delta \mathbf{r})}_{\text{Coil Sensitivity}} \times \underbrace{\exp(j \Delta \mathbf{CS}_{i_{\text{CS}}} \text{TE}_{i_{\text{TE}}})}_{\text{Chemical Shift}} \times \underbrace{\exp(j \Delta \mathbf{B0}_{i_r} t_{i_k})}_{\text{Off-Resonance}}.$$

where the k-space vector and the spatial coordinates were modified as  $\mathbf{k}_{i_k} \rightarrow \mathbf{k}'_{i_k, i_r}$  and  $\mathbf{r}_{i_r} \rightarrow \mathbf{r}_{i_r} + \Delta \mathbf{r}$  respectively to include gradient imperfections and rigid-body motion. The data was also undersampled (acceleration factor  $2 \times 2$ ) with the inclusion of the coil sensitivity encoding in the column 4. Row 4 shows reconstruction using **Encode** accounting for Gradient encoding only, and row 5 shows reconstruction with all relevant encoding accounted for.

In addition to the encoding examples highlighted here, other forms of desired and undesired encoding may also be included [33, 34, 35, 36], for example simultaneous multi-slice imaging and spatially varying relaxation decay.

## 4 Exemplary Applications

Several emerging MRI applications feature small to medium matrix sizes and could benefit from non-FFT-based reconstruction, making them good candidates for Pinv-Recon. Examples include hyperpolarized MRI [37], diffusion MRI [38], certain functional MRI acquisitions [39], multi-nuclear spectroscopic imaging [40], and low-field MRI [41]. These often have low SNR and use non-Cartesian trajectories or require distortion corrections, which are challenging for traditional FFT-based pipelines but are naturally handled in the explicit encoding matrix formulation. In the following subsections, we demonstrate Pinv-Recon in various experimental scenarios, beginning with smaller image sizes, and then pushing to larger matrix sizes to show the possibilities of Pinv-Recon. Additional examples are shown in Supplementary Materials 3 and 4.

### 4.1 Low Resolution 2D Spectral-Spatial Spiral (Hyperpolarized Carbon-13 MRI)

As shown in Fig. 4, we first applied Pinv-Recon to an 8-channel hyperpolarized  $^{13}\text{C}$  metabolic imaging dataset acquired with a 2D spiral trajectory (MTX  $20 \times 20$ ) [42].

Data was reconstructed using (1) Pinv-Recon with gradient encoding only and root-sum-of-squares coil combination, (2) Pinv-Recon with coil sensitivity encoding included, as well as (3) Pinv-Recon with coil sensitivity encoding and overdiscretization to a higher-resolution spatial grid of MTX  $64 \times 64$ . Since the coil sensitivity is spatially-varying but time-invariant, the reconstruction matrix has to be calculated for each of the eight individual slices, but can be used to reconstruct the images across all time points and metabolites in eight matrix-matrix multiplications. Including the coil sensitivity profiles allowed for a more SNR-optimal combination than simple root-sum-of-squares coil combination. Overdiscretized reconstruction can be straightforwardly implemented by defining a finer range of  $\mathbf{r}$  (equation (2)), which is much simpler compared to over-discretized reconstruction using gridding, often applied by interpolating the data to a finer Cartesian grid [4, 43]. Pinv-Recon also allowed the calculation of the SRF and noise maps demonstrating that inclusion of the coil sensitivities improves the SRF. Moreover, Pinv-Recon provides inherent and

straightforward denoising by regularization, either by truncation of the SVD or by Tikhonov regularization, which is especially useful for SNR-limited techniques such as hyperpolarized carbon-13 imaging [44].

## 4.2 Medium Resolution 3D Stack-of-Spirals (Hyperpolarized Xenon-129 MRI)

As shown in Fig. 5, a hyperpolarized Xenon-129 dataset (acquired using a golden-angle stack-of-spirals with MTX  $80 \times 80 \times 41$ ) demonstrates Pinv-Recon at a larger matrix size and with a separable Z-dimension. This is an example of non-Cartesian in-plane sampling combined with Cartesian phase-encoding along Z with a single slab-selection pulse. In reconstruction, the uniformly sampled Z-dimension was factored out, and Pinv-Recon was separately applied to the non-uniformly sampled in-plane 2D spiral. Reconstruction at the native resolution and over-discretized to twice the resolution can be performed at reasonable compute times of just a couple of seconds using Cholesky decomposition.

Pinv-Recon was also compared against several methods: (1)  $CG_{Encode}$ , (2) non-uniform FFT (NUFFT) reconstruction [45] (3) NUFFT reconstruction with additional regularization, and (4) conventional gridding. The benefit of inherent regularization in Pinv-Recon is highlighted, allowing better reconstruction of ill-conditioned undersampled data [46]. The golden-angle spiral trajectory had unevenly-spaced interleaves, creating voids in k-space that translate to density compensation factors larger than unity. This creates an ill-posed problem which gridding algorithms may not be able to solve properly without regularization. Streaking artifacts that were present in the gridding and the NUFFT reconstructed images can be minimized with additional regularization. However, this is inherently accounted for in the Pinv-Recon and  $CG_{Encode}$  implementations with Tikhonov Regularization included.

The SRF (Fig. 5c, top row) and the noise matrix (Fig. 5c, bottom row) for the reconstruction of the hyperpolarized Xenon image can be calculated for tSVD and Tikhonov regularization respectively, showing that the image is less well-represented and less noisy towards the center of the image with this level of Tikhonov regularization.

## 4.3 High Resolution 2D Cartesian VDPD ( $T_2$ -weighted Knee)

We further demonstrate the efficiency of Pinv-Recon for separable imaging dimensions, using a high resolution 18-channel 2D Variable Density Poisson Disk (VDPD) knee dataset (MTX  $384 \times 336$ ), which is evenly sampled in the readout dimension, but variably sampled in the phase encoding dimension (Fig. 6). The dataset undersamples k-space in the phase encoding dimension with an acceleration factor (R) of around 3. Along the frequency encoding line, each phase encode is reconstructed separately, accounting for coil sensitivity.

We show that by incorporating the coil sensitivity profiles, a higher resolution and more accurate image can be reconstructed by ameliorating pseudo-random sub-sampling artifacts (Fig. 6c). From the corresponding SRF map with values close to 1 (Fig. 6f), it can be seen that almost full nominal image resolution can be recovered, in contrast to the gradient-encoding-only SRF map with values of around 0.3 (Fig. 6e).

#### 4.4 High Resolution 2D Radial with Undersampling (CG-SENSE Challenge Dataset)

We explored the application of Pinv-Recon to even larger matrix sizes, demonstrating its computational feasibility using the widely recognized open-source radial brain dataset from the ISMRM CG-SENSE reproducibility challenge [13]. Using this dataset, we show that a MTX  $320 \times 320$  image can be reconstructed in just a few minutes, with the possibility of including non-Cartesian SENSE reconstruction for undersampled data. The dimensionality of the encoding matrix can be reduced by masking out image voxels beyond the field-of-view of interest.

Instead of using forward and inverse gridding or NUFFT to iteratively reconstruct the image, we demonstrate the computational feasibility of Pinv-Recon as an alternative to non-Cartesian SENSE by simply incorporating the coil sensitivity into the encoding matrix and pseudoinverting it. Reconstruction with acceleration factors of  $R = 1$  to 4 are shown in Fig. 7.  $CG_{Encode}$  gives a similar image to Pinv-Recon but does not straightforwardly provide the SRFs and noise maps (columns 4 and 5 in Fig. 7). Especially in the context of non-Cartesian undersampled reconstruction, these metrics provide valuable information about the optimality of encoding and reconstruction. Using the SVD, whilst computationally more expensive than other matrix decomposition methods, can still be useful for shedding light onto the conditioning of the problem, as shown in the rightmost panel of Figure 7.

#### 4.5 High Resolution 3D Stack-of-Stars (Abdominal Imaging)

Separable 3D Pinv-Recon was demonstrated using a high-resolution abdominal 3D stack-of-stars Liver acquisition with volume acceleration (Fig. 8) which has MTX  $320 \times 320 \times 144$ . Similar to the ISMRM CG-SENSE reproducibility challenge, only image pixels in the masked region are included in reconstruction. The Z phase-encoding dimension was factored out, and the XY dimensions were reconstructed using Pinv-Recon, forming a 3D image which is shown in the leftmost column in axial, coronal and sagittal views.

The potential for real-time image reconstruction, i.e., updating the reconstructed image during scanning, is demonstrated in this dataset. Unlike gridding and iterative reconstruction methods, Pinv-Recon is data agnostic in that the reconstruction matrix can be calculated simply using the known trajectory, even before data is acquired. Once data acquisition finishes, only a simple matrix-vector reconstruction remains. The top row of Fig. 8 shows images obtained using increasing fractions of the available data spokes from left to right, indicating the potential for real-time updates during imaging. The acquisition time of certain MRI scans can last up to several minutes (6 minutes for this dataset), and real-time updates can be useful for radiographers or scanner operators to monitor the acquisition.

Comparison of Pinv-Recon and  $CG_{Encode}$  is shown in the bottom two rows of Fig. 8. The middle row shows images obtained using varying thresholds for Pinv-Recon with tSVD, demonstrating the trade-off between resolution and SNR offered by varying the condition number  $\kappa$ , also illustrated in the SVD spectrum on the right. The bottom row shows images reconstructed using  $CG_{Encode}$ . As is common with CG-based iterative methods, image quality first improves, peaks and then degrades with an increasing number of iterations.



## 5 Discussion

With the drastic increase in computational power over the past two decades [47], inverting large encoding matrices has become much more feasible. For example, Van de Walle *et al.* (2000) reported approximately 75 minutes to reconstruct a MTX  $64 \times 64$  image ( $N_k \times N_r = 64^2 \times 4033$ ) [11]; today, the same size matrix can be decomposed in seconds (approximately 2 s with SVD or less than 0.1 s with Cholesky on our workstation). In our experiments, a  $\sim 2$  GB encoding matrix (roughly equivalent to a MTX  $128 \times 128$  image with full Fourier encoding) was inverted via Cholesky Decomposition in about 0.4 s. Memory limitations, a major barrier in the past, are far less restrictive on modern 64-bit systems that can address terabytes of RAM [12, 48]. Looking forward, ongoing developments in high-performance computing architectures and half-precision arithmetic promise to further extend the capabilities of Pinv-Recon [49, 50].

Among the matrix inversion methods examined, SVD is the most robust and provides valuable insight (via the SVD spectrum) into the conditioning of the problem [11, 51]. However, SVD is computationally expensive. Our exploration of alternative factorizations revealed that many of these methods, though not previously considered in MRI reconstruction, can offer substantial speed-ups. In particular, Cholesky decomposition was observed to be over  $100\times$  faster than SVD in some cases. These methods operate on the normal equations (decomposing the Gram matrix), effectively reducing the problem size to the smaller dimension of **Encode**. Utilization of block matrix operations to perform block-wise inversion allows further leverage of GPU resources even for large encoding matrices. Regularization, straightforwardly implemented in an interpretable manner using either tSVD or Tikhonov regularization in Pinv-Recon, is also beneficial for minimizing noise and for solving ill-conditioned, undersampled problems as demonstrated by our Xenon-129 dataset.

Perhaps the greatest strength of Pinv-Recon is its versatility and simplicity. It seamlessly accommodates non-Cartesian trajectories and a variety of corrections that would otherwise require complex dedicated algorithms [5, 52, 53, 54]. Conventional reconstruction pipelines often involve multiple stages (e.g., density compensation [55, 56], trajectory correction, off-resonance modulation, motion gating, coil combination, deapodization, gradient nonlinearity correction), each adding complexity and variability. Many of these algorithms cannot be easily combined with one another. In Pinv-Recon, all these effects are incorporated into the single encoding matrix, thereby simplifying the reconstruction workflow and improving reproducibility. This builds upon previous work using the explicit encoding matrix in conjugate-gradient methods, for example Wilm *et al.*'s *Higher order reconstruction for MRI in the presence of spatiotemporal field perturbations* [23]. Leveraging modern compute resources, Pinv-Recon implements this more simply, and also calculates **Recon** to provide, by simple matrix-matrix multiplication, additional metrics such as SRF maps and noise amplification maps that can serve as quality assurance measures and guide future sequence design [14, 26, 57, 58, 59].

With the move towards open-source and reproducible MR acquisition and reconstruction, as evidenced by the growing popularity of the vendor-neutral pulse sequence programming environment Pulseq, Pinv-Recon shows great promise as a simple, versatile, and reliable reconstruction method [60, 61]. An example implementation of Pinv-Recon for Pulseq is now available and can be found at [62]. Researchers developing novel reconstruction techniques may use Pinv-Recon as a reference reconstruction method since it provides the generic linear-least squares solution (or the minimum 2-norm solution for underdetermined cases). Moreover, Pinv-Recon can also be used as an instructive educational tool for students familiarizing themselves with various aspects of MR physics, exploiting its modularity to visualize each encoding mechanism.

We acknowledge that Pinv-Recon is not intended to replace all FFT-based or iterative methods; rather, it excels in small to medium matrix size applications (up to approximately  $256 \times 256$  in-plane) where its computational burden is manageable and its advantages in flexibility and reproducibility are most pronounced. For very high-resolution imaging, iterative methods may remain more practical.

In conclusion, we have shown that direct pseudoinversion of the encoding matrix—once considered impractical—is now within reach for many MR reconstruction problems. Pinv-Recon leverages modern computational resources and optimized linear algebra routines to provide a simple, linear, and extendable reconstruction framework that is particularly well-suited for MRI applications with small to medium matrix sizes and specialized encoding requirements. The presented framework can unify multiple linear encoding strategies and correction mechanisms into a single, comprehensive algebraic model. This one-step approach not only computes the image directly but also yields valuable image metrics such as spatial response functions and noise maps, and has the potential for real-time feedback during imaging, making it a valuable tool for both research and clinical applications.

## 6 Methods

### 6.1 Computational Evaluation and Numerical Simulations

The computational evaluation and numerical simulations were performed as described in Section 3, using Matlab 2023b (The MathWorks, MA, USA). The MATLAB implementation can be also found in the Git repository linked in the Data Availability Statement.

### 6.2 Applications

All reconstructions were performed using the equations outlined in Section 2. Details of the acquisition of each dataset are as follows:

**Hyperpolarized Carbon-13 Dataset:** A healthy volunteer was scanned after IV injection of 35 mL of hyperpolarized  $[1-^{13}\text{C}]$ pyruvate (polarized for approximately 4 hours in the SPINlab (GE Healthcare, WI, USA)). The acquisition was a spectral-spatial single-arm spiral sequence covering a  $240 \times 240$  mm field-of-view with eight 20 mm slices; flip angles were  $5^\circ$  for pyruvate,  $15^\circ$  for lactate, and  $60^\circ$  for bicarbonate, acquired at 4 s intervals. The scan was performed on a GE 3T Premier (GE Healthcare, WI, USA) system using an 8-channel transmit-receive  $^{13}\text{C}/^1\text{H}$  head coil (Rapid Biomedical, Rimpf, Germany). Coil sensitivity maps were estimated via polynomial smoothing of pyruvate images from each individual coil and normalized by the sum-of-squares of all coils. This project was approved by the University of Nottingham Medical School Ethics Committee (Ref: 416-1911 BRAIN DNP) and was conducted in accordance with the standards set by the latest version of the Declaration of Helsinki, except for registration in a database. Informed, written consent was obtained from the volunteer before participation.

**Hyperpolarized Xenon-129 Dataset:** A healthy 34-year-old female participant inhaled 1 L of enriched  $^{129}\text{Xe}$  gas (polarized for approximately 30 minutes). Imaging was performed on a 3T GE Premier scanner with a flexible  $^{129}\text{Xe}$  chest coil (PulseTeq, Cobham, UK) using a stack-of-spirals 3D sequence covering a  $400 \times 400 \times 200$  mm field-of-view. The sequence employed 16 spiral interleaves with golden-angle rotation, a bandwidth of 250 kHz,  $\text{TR} = 15.6$  ms,  $\text{TE} = 2.3$  ms, and a hard excitation pulse yielding an effective flip angle of approximately  $66^\circ$  per volume.

Participants gave informed written consent, and ethics approval was provided by the University of Oxford Central University Research Ethics Approval (Reference: R77150/RE001).

Pinv-Recon of the dataset was compared with conjugate gradient iterative reconstruction with 11 iterations, NUFFT using the Michigan Image Reconstruction Toolbox (MIRT) [45] (density compensation calculated using the Pipe and Menon method [63], NUFFT object calculated with min-max interpolator with Kaiser-Bessel scaling, kernel width of 6, table-based interpolation with a  $2^{10}$  oversampling factor) without and with additional regularization with quadratic penalized weighted least squares (10 iterations, with a beta of  $2^{-21}$ ), and conventional gridding (Kaiser-Bessel filtering [4] with kernel width of 3 and oversampling to 1.125 of the original grid size, density compensation factor determined using Voronoi triangulation).

**$T_2$ -weighted Knee:** The knee dataset was acquired with a dedicated knee coil with 18 receive channels using a 2D fast recovery fast spin echo (frFSE) acquisition with fat saturation. The acquisition parameters were TR = 6 s, TE = 108 ms. The trajectory was a 1D variable density poison disc (VDPD) sampling with image matrix size of 384 in the readout direction and 336 in the phase encoding direction. The phase encoding dimension was acquired with 3.23 acceleration (104/336), and the center of k-space (-12:12) was fully sampled for coil sensitivity calibration.

**ISMRM CG-SENSE Challenge Dataset:** The ISMRM CG-SENSE Challenge dataset was obtained from *CG-SENSE revisited: Results from the first ISMRM reproducibility challenge* [13].

**LAVA-Star Abdominal dataset:** For the 3D stack-of-stars dataset, the acquisition parameters were FOV =  $40.0 \times 40.0 \times 31.68$  cm, resolution =  $1.25 \times 1.25 \times 2.2$  mm, TE/TR = 1.488/3.276 ms, FA =  $12^\circ$ , BW =  $\pm 62.5$  kHz, with interleaved fat suppression, resulting in a scan time of 5 min 58 sec.

## References

- [1] Andrew Webb and Johnes Obungoloch. Five steps to make MRI scanners more affordable to the world. *Nature*, 615(7952):391–393, March 2023.
- [2] P. C. Lauterbur. Image Formation by Induced Local Interactions: Examples Employing Nuclear Magnetic Resonance. *Nature*, 242(5394):190–191, March 1973.
- [3] Robert R Edelman. The history of MR imaging as seen through the pages of radiology. *Radiology*, 273(2).
- [4] Philip J. Beatty, Dwight G. Nishimura, and John M. Pauly. Rapid gridding reconstruction with a minimal oversampling ratio. *IEEE transactions on medical imaging*, 24(6):799–808, June 2005.
- [5] Katherine L. Wright, Jesse I. Hamilton, Mark A. Griswold, Vikas Gulani, and Nicole Seiberlich. Non-Cartesian parallel imaging reconstruction. *Journal of Magnetic Resonance Imaging*, 40(5):1022–1040, 2014.
- [6] Lai-Chee Man, John M. Pauly, and Albert Macovski. Multifrequency interpolation for fast off-resonance correction. *Magnetic Resonance in Medicine*, 37(5):785–792, 1997.
- [7] Klaas P. Pruessmann, Markus Weiger, Peter Börnert, and Peter Boesiger. Advances in sensitivity encoding with arbitrary k-space trajectories. *Magnetic Resonance in Medicine*, 46(4):638–651, 2001.

- [8] Dao-Qi Chen, Robert B. Marr, and Paul C. Lauterbur. Reconstruction from NMR Data Acquired with Imaging Gradients Having Arbitrary Time Dependence. *IEEE Transactions on Medical Imaging*, 5(3):162–164, September 1986.
- [9] Y.M. Kadah and Xiaoping Hu. Algebraic reconstruction for magnetic resonance imaging under B/sub 0/ inhomogeneity. *IEEE Transactions on Medical Imaging*, 17(3):362–370, June 1998.
- [10] Gastao Cruz, Burhaneddin Yaman, Mehmet Akçakaya, Mariya Doneva, and Claudia Prieto. Chapter 2 - MRI Reconstruction as an Inverse Problem. In Mehmet Akçakaya, Mariya Doneva, and Claudia Prieto, editors, *Advances in Magnetic Resonance Technology and Applications*, volume 7 of *Magnetic Resonance Image Reconstruction*, pages 37–57. Academic Press, January 2022.
- [11] R. Van De Walle, H.H. Barrett, K.J. Myers, M.I. Aitbach, B. Desplanques, A.F. Gmitro, J. Cornelis, and I. Lemahieu. Reconstruction of MR images from data acquired on a general nonregular grid by pseudoinverse calculation. *IEEE Transactions on Medical Imaging*, 19(12):1160–1167, December 2000.
- [12] Shuangbao Paul Wang. Computer Memory and Storage. In Shuangbao Paul Wang, editor, *Computer Architecture and Organization: Fundamentals and Architecture Security*, pages 45–69. Springer, Singapore, 2021.
- [13] Oliver Maier, Steven Hubert Baete, Alexander Fyrdahl, Kerstin Hammernik, Seb Harreveld, Lars Kasper, Agah Karakuzu, Michael Loecher, Franz Patzig, Ye Tian, Ke Wang, Daniel Gallichan, Martin Uecker, and Florian Knoll. CG-SENSE revisited: Results from the first ISMRM reproducibility challenge. *Magnetic Resonance in Medicine*, 85(4):1821–1839, 2021.
- [14] K. P. Pruessmann, M. Weiger, M. B. Scheidegger, and P. Boesiger. SENSE: Sensitivity encoding for fast MRI. *Magnetic Resonance in Medicine*, 42(5):952–962, November 1999.
- [15] João Carlos Alves Barata and Mahir Saleh Hussein. The Moore–Penrose Pseudoinverse: A Tutorial Review of the Theory. *Brazilian Journal of Physics*, 42(1):146–165, April 2012.
- [16] Thomas Kirchner, Ariane Fillmer, Jeffrey Tsao, Klaas Paul Pruessmann, and Anke Henning. Reduction of voxel bleeding in highly accelerated parallel 1H MRSI by direct control of the spatial response function. *Magnetic Resonance in Medicine*, 73(2):469–480, 2015.
- [17] Gene H. Golub and Charles F. Van Loan. *Matrix Computations*. JHU Press, February 2013.
- [18] Walter Gander. Algorithms for the QR decomposition. *Res. Rep.*, 80(02):1251–1268, 1980.
- [19] A. N. Tikhonov and V. Y. Arsenin. *Solutions of Ill-Posed Problems*. Scripta Series in Mathematics. Winston and distributed solely by Halsted Press, 1977.
- [20] Per Christian Hansen and Dianne Prost O’Leary. The Use of the L-Curve in the Regularization of Discrete Ill-Posed Problems. *SIAM Journal on Scientific Computing*, 14(6):1487–1503, November 1993.
- [21] John Pauly. Chapter 5 - Reconstruction of Non-Cartesian Data, 2005. [https://users.fmrib.ox.ac.uk/~karla/reading\\_group/lecture\\_notes/AdvRecon\\_Pauly\\_read.pdf](https://users.fmrib.ox.ac.uk/~karla/reading_group/lecture_notes/AdvRecon_Pauly_read.pdf).

- [22] Chapter 5: Tikhonov regularization. In *Linear and Nonlinear Inverse Problems with Practical Applications*, Computational Science & Engineering, pages 63–82. Society for Industrial and Applied Mathematics, October 2012.
- [23] Bertram J. Wilm, Christoph Barmet, Matteo Pavan, and Klaas P. Pruessmann. Higher order reconstruction for MRI in the presence of spatiotemporal field perturbations. *Magnetic Resonance in Medicine*, 65(6):1690–1701, 2011.
- [24] Shu Li, Cheong Chan, Jason P. Stockmann, Hemant Tagare, Ganesh Adluru, Leo K. Tam, Gigi Galiana, R. Todd Constable, Sebastian Kozerke, and Dana C. Peters. Algebraic reconstruction technique for parallel imaging reconstruction of undersampled radial data: Application to cardiac cine. *Magnetic Resonance in Medicine*, 73(4):1643–1653, April 2015.
- [25] Klaas P. Pruessmann. Encoding and reconstruction in parallel MRI. *NMR in biomedicine*, 19(3):288–299, May 2006.
- [26] Javier Sánchez-González, Jeffrey Tsao, Ulrike Dydak, Manuel Desco, Peter Boesiger, and Klaas Paul Pruessmann. Minimum-norm reconstruction for sensitivity-encoded magnetic resonance spectroscopic imaging. *Magnetic Resonance in Medicine*, 55(2):287–295, February 2006.
- [27] Florian Wiesinger, Eliane Weidl, Marion I. Menzel, Martin A. Janich, Oleksandr Khagai, Steffen J. Glaser, Axel Haase, Markus Schwaiger, and Rolf F. Schulte. IDEAL spiral CSI for dynamic metabolic MR imaging of hyperpolarized [1-13C]pyruvate. *Magnetic Resonance in Medicine*, 68(1):8–16, 2012.
- [28] Melissa W. Haskell, Jon-Fredrik Nielsen, and Douglas C. Noll. Off-resonance artifact correction for MRI: A review. *NMR in Biomedicine*, 36(5):e4867, 2023.
- [29] J. H. Duyn, Y. Yang, J. A. Frank, and J. W. van der Veen. Simple correction method for k-space trajectory deviations in MRI. *Journal of Magnetic Resonance (San Diego, Calif.: 1997)*, 132(1):150–153, May 1998.
- [30] Jürgen Rahmer, Peter Mazurkewitz, Peter Börnert, and Tim Nielsen. Rapid acquisition of the 3D MRI gradient impulse response function using a simple phantom measurement. *Magnetic Resonance in Medicine*, 82(6):2146–2159, 2019.
- [31] Christoph Barmet, Nicola De Zanche, and Klaas P. Pruessmann. Spatiotemporal magnetic field monitoring for MR. *Magnetic Resonance in Medicine*, 60(1):187–197, 2008.
- [32] Pekka Sipilä, Sebastian Greding, Gerhard Wachutka, and Florian Wiesinger. 2H transmit–receive NMR probes for magnetic field monitoring in MRI. *Magnetic Resonance in Medicine*, 65(5):1498–1506, 2011.
- [33] K. F. King and L. Angelos. SENSE image quality improvement using matrix regularization. In *Proceedings of the 9th Annual Meeting of ISMRM, Glasgow, Scotland*, page 1771, 2001.
- [34] A. A. Maudsley. Fourier imaging using rf phase encoding. *Magnetic Resonance in Medicine*, 3(5):768–777, 1986.

- [35] Ralf Kartäusch, Toni Driessle, Thomas Kampf, Thomas Christian Basse-Lüsebrink, Uvo Christoph Hoelscher, Peter Michael Jakob, Florian Fidler, and Xavier Helluy. Spatial phase encoding exploiting the Bloch–Siegert shift effect. *Magnetic Resonance Materials in Physics, Biology and Medicine*, 27(5):363–371, October 2014.
- [36] Laura I. Sacolick, Florian Wiesinger, Ileana Hancu, and Mika W. Vogel. B1 mapping by Bloch–Siegert shift. *Magnetic Resonance in Medicine*, 63(5):1315–1322, 2010.
- [37] Peder Eric Zufall Larson and Jeremy W. Gordon. Hyperpolarized Metabolic MRI—Acquisition, Reconstruction, and Analysis Methods. *Metabolites*, 11(6):386, June 2021.
- [38] Valerij G. Kiselev. Fundamentals of diffusion MRI physics. *NMR in Biomedicine*, 30(3):e3602, 2017.
- [39] Luis Hernandez-Garcia, Anish Lahiri, and Jonas Schollenberger. Recent progress in ASL. *NeuroImage*, 187:3–16, February 2019.
- [40] Yi Wei, Caiwei Yang, Hanyu Jiang, Qian Li, Feng Che, Shang Wan, Shan Yao, Feifei Gao, Tong Zhang, Jiazheng Wang, and Bin Song. Multi-nuclear magnetic resonance spectroscopy: State of the art and future directions. *Insights into Imaging*, 13(1):135, August 2022.
- [41] Thomas Campbell Arnold, Colbey W. Freeman, Brian Litt, and Joel M. Stein. Low-field MRI: Clinical promise and challenges. *Journal of Magnetic Resonance Imaging*, 57(1):25–44, 2023.
- [42] Rolf F. Schulte, Jonathan I. Sperl, Eliane Weidl, Marion I. Menzel, Martin A. Janich, Oleksandr Khagai, Markus Durst, Jan Henrik Ardenkjaer-Larsen, Steffen J. Glaser, Axel Haase, Markus Schwaiger, and Florian Wiesinger. Saturation-recovery metabolic-exchange rate imaging with hyperpolarized [1-<sup>13</sup>C] pyruvate using spectral-spatial excitation. *Magnetic Resonance in Medicine*, 69(5):1209–1216, 2013.
- [43] H. Schomberg and J. Timmer. The gridding method for image reconstruction by Fourier transformation. *IEEE Transactions on Medical Imaging*, 14(3):596–607, September 1995.
- [44] Yaewon Kim, Hsin-Yu Chen, Adam W. Autry, Javier Villanueva-Meyer, Susan M. Chang, Yan Li, Peder E. Z. Larson, Jeffrey R. Brender, Murali C. Krishna, Duan Xu, Daniel B. Vigneron, and Jeremy W. Gordon. Denoising of hyperpolarized <sup>13</sup>C MR images of the human brain using patch-based higher-order singular value decomposition. *Magnetic Resonance in Medicine*, 86(5):2497–2511, 2021.
- [45] Jeffrey A. Fessler. Michigan Image Reconstruction Toolbox (MIRT). <https://web.eecs.umich.edu/~fessler/code/>, 0000.
- [46] Martin Uecker, Shuo Zhang, Dirk Voit, Alexander Karaus, Klaus-Dietmar Merboldt, and Jens Frahm. Real-time MRI at a resolution of 20 ms. *NMR in Biomedicine*, 23(8):986–994, 2010.
- [47] GE Moore. Cramming More Components onto Integrated Circuits. *Electronics*, 38(8):1–14, 1965.
- [48] Mathworks. Table of Matlab release features, 2024. <https://uk.mathworks.com/matlabcentral/discussions/general/847991-table-of-matlab-release-features>.

- [49] NVIDIA. NVIDIA Blackwell Architecture, 0000. <https://www.nvidia.com/en-us/data-center/technologies/blackwell-architecture/>.
- [50] Cerebras. Product - Chip., 2024. <https://cerebras.ai/product-chip/>.
- [51] B. Desplanques, D.J. Cornelis, E. Achten, R. Van De Walle, and I. Lemahieu. Iterative reconstruction of magnetic resonance images from arbitrary samples in k-space. *IEEE Transactions on Nuclear Science*, 49(5):2268–2273, October 2002.
- [52] Kangrong Zhu, Robert F. Dougherty, Hua Wu, Matthew J. Middione, Atsushi M. Takahashi, Tao Zhang, John M. Pauly, and Adam B. Kerr. Hybrid-Space SENSE Reconstruction for Simultaneous Multi-Slice MRI. *IEEE transactions on medical imaging*, 35(8):1824–1836, August 2016.
- [53] Kevin D. Harkins, Mark D. Does, and William A. Grissom. Iterative Method for Predistortion of MRI Gradient Waveforms. *IEEE Transactions on Medical Imaging*, 33(8):1641–1647, August 2014.
- [54] Martin Uecker, Peng Lai, Mark J. Murphy, Patrick Virtue, Michael Elad, John M. Pauly, Shreyas S. Vasanawala, and Michael Lustig. Espirit — an eigenvalue approach to autocalibrating parallel mri: Where sense meets grappa. *Magnetic resonance in medicine*, 71(3):990–1001, 2014.
- [55] V. Rasche, R. Proksa, R. Sinkus, P. Börnert, and H. Eggers. Resampling of data between arbitrary grids using convolution interpolation. *IEEE transactions on medical imaging*, 18(5):385–392, May 1999.
- [56] Hao Tan and Yibin Zheng. Point spread function optimization for MRI reconstruction. In *Proceedings. (ICASSP '05). IEEE International Conference on Acoustics, Speech, and Signal Processing, 2005.*, volume 2, pages ii/477–ii/480 Vol. 2, March 2005.
- [57] P. B. Roemer, W. A. Edelstein, C. E. Hayes, S. P. Souza, and O. M. Mueller. The NMR phased array. *Magnetic Resonance in Medicine*, 16(2):192–225, 1990.
- [58] Peter Kellman and Elliot R. McVeigh. Image reconstruction in SNR units: A general method for SNR measurement. *Magnetic Resonance in Medicine*, 54(6):1439–1447, December 2005.
- [59] Elizabeth Mary Tunnicliffe, Martin John Graves, and Matthew D Robson. Use of the Noise Covariance Matrix in Array Coil Quality Assurance. In *Proceedings of the International Society for Magnetic Resonance in Medicine*, Montreal, Quebec, Canada, 2011.
- [60] Kelvin J. Layton, Stefan Kroboth, Feng Jia, Sebastian Littin, Huijun Yu, Jochen Leupold, Jon-Fredrik Nielsen, Tony Stöcker, and Maxim Zaitsev. Pulseseq: A rapid and hardware-independent pulse sequence prototyping framework. *Magnetic Resonance in Medicine*, 77(4):1544–1552, 2017.
- [61] Marten Veldmann, Philipp Ehse, Kelvin Chow, Jon-Fredrik Nielsen, Maxim Zaitsev, and Tony Stöcker. Open-source MR imaging and reconstruction workflow. *Magnetic Resonance in Medicine*, 88(6):2395–2407, 2022.

- [62] Jon-Fredrik Nielsen. SequenceExamples-GE/pge2/spiral at main · HarmonizedMRI/SequenceExamples-GE, 2025. <https://github.com/HarmonizedMRI/SequenceExamples-GE/tree/main/pge2/spiral>.
- [63] James G. Pipe and Padmanabhan Menon. Sampling density compensation in MRI: Rationale and an iterative numerical solution. *Magnetic Resonance in Medicine*, 41(1):179–186, 1999.

## Funding Declaration

K.Y. acknowledges an Oxford-Medical Research Council Doctoral Training Partnership iCASE award, the Oxford-Radcliffe Scholarship, and GE HealthCare for graduate funding. D.J.T. was funded by a British Heart Foundation Senior Basic Science Research Fellowship (FS/19/18/34252). J.T.G. is funded by the Oxford Biomedical Research Centre, and acknowledges the BHF Centre of Research Excellence, University of Oxford for funding. The hyperpolarized Xenon-129 datasets were funded by the British Heart Foundation (RE/18/3/34214) and the hyperpolarized Carbon-13 dataset was funded by Nottingham Life cycle 5.

## Author Contributions Statement

K.Y.: writing - original draft (lead); conceptualization (supporting); data collection (equal); methodology (equal); software (equal); formal analysis (equal); writing - review and editing (equal). C.T.: conceptualization (supporting); writing - review and editing (equal). R.F.S.: conceptualization (supporting); writing - review and editing (equal). B.W.: visualization; writing - review and editing (equal). A.M.: data collection (equal). S.S.: data collection (equal); writing - review and editing (equal). P.M.: data collection (equal). D.A.: data collection (equal). F.V.G.: funding acquisition (equal); supervision. D.J.T.: funding acquisition (equal); supervision (equal); writing - review and editing (equal). J.T.G.: funding acquisition (equal); supervision (equal); writing - review and editing (equal). F.W.: conceptualization (lead); writing - original draft (supporting); methodology (equal); software (equal); formal analysis (equal); supervision (equal); writing - review and editing (equal). All authors read and approved the final manuscript.

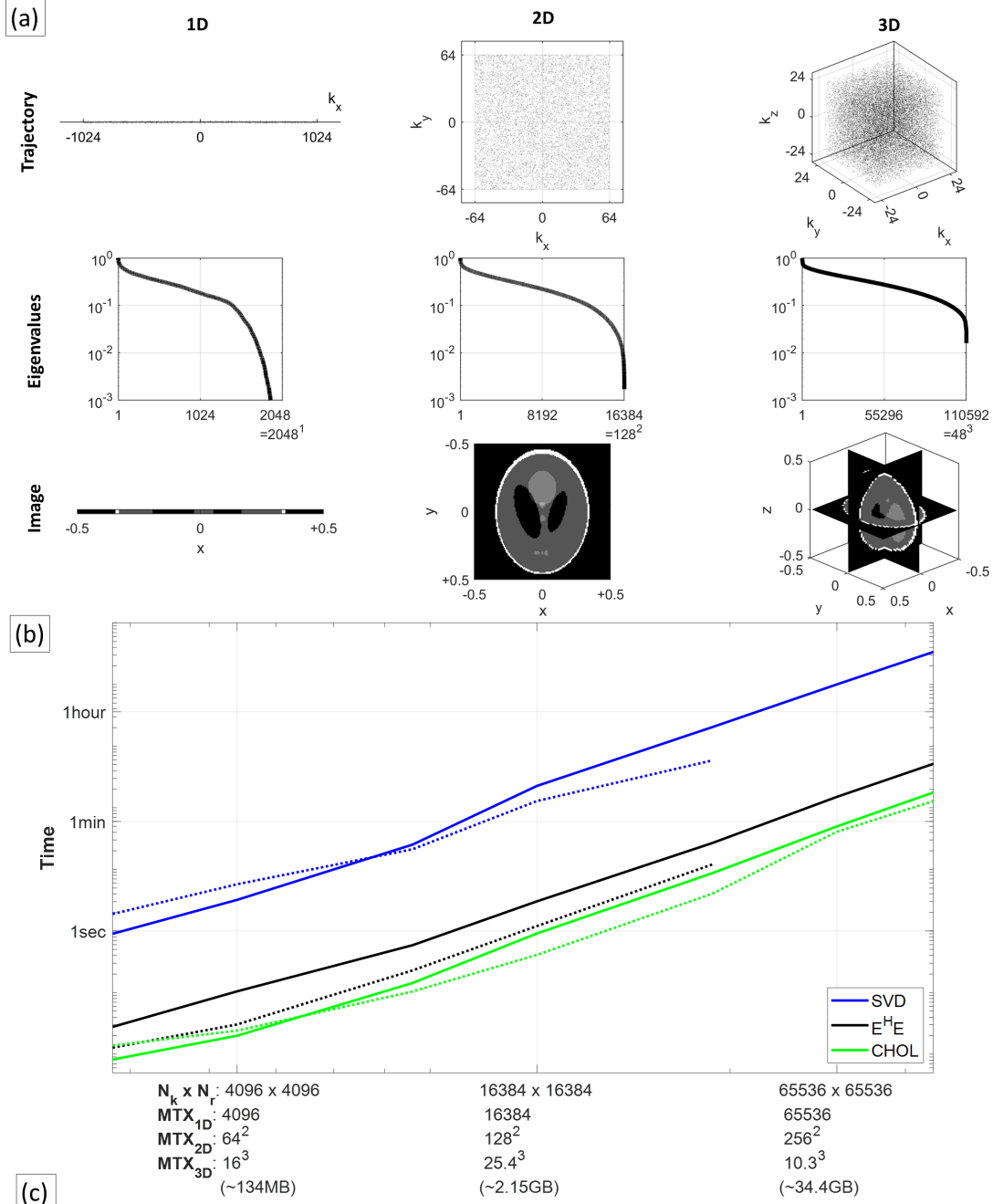
## Competing Interests Statement

C.T. is an employee of The Mathworks. R.F.S. and F.W. are employees of GE HealthCare. S.S. is an Editorial Board Member of *Scientific Reports*. The remaining authors declare no relevant conflicts of interest.

## Data Availability Statement

The code supporting the numerical simulations in this manuscript, as well as some example datasets can be found at <https://github.com/univ39/Pinv-Recon>.





$N_k \times N_r$	4096 x 4096		9216 x 9216		16384 x 16384		36864 x 36864		65536 x 65536		102400 x 102400	
Memory [GB] (single precision)	0.13		0.67		2.14		10.87		34.35		83.88	
	CPU	GPU	CPU	GPU	CPU	GPU	CPU	GPU	CPU	GPU	CPU	GPU
SVD	0.151	0.395	3.198	5.733	226.254	128.521	2038.423	586.429	10040.230		33802.053	
QR	0.050	0.084	0.658	1.547	66.958	25.973	658.021	150.383	3787.878		21007.858	
EHE	0.004	0.004	0.105	0.030	3.030	1.202	26.777	12.030	150.183		516.710	
Eig	0.096	0.191	1.853	0.947	103.276	13.186	994.070	128.407	5316.127		15876.709	
Chol	0.002	0.006	0.020	0.024	0.912	0.410	8.690	4.039	49.800	40.80*	177.302	128.09*

Figure 1: (a) Illustrations of PinV-Recon using generic 1D, 2D and 3D trajectories. (b) Plot of computational times for SVD, computing  $\mathbf{E}^H \mathbf{E}$ , and Cholesky decomposition for a range of matrix sizes using CPU only (solid lines) and with GPU acceleration (dotted lines) (c) Corresponding table of computational times also including QR and Eigenvalue decomposition. Asterisks (\*) indicate decomposition using block-wise Cholesky decomposition.

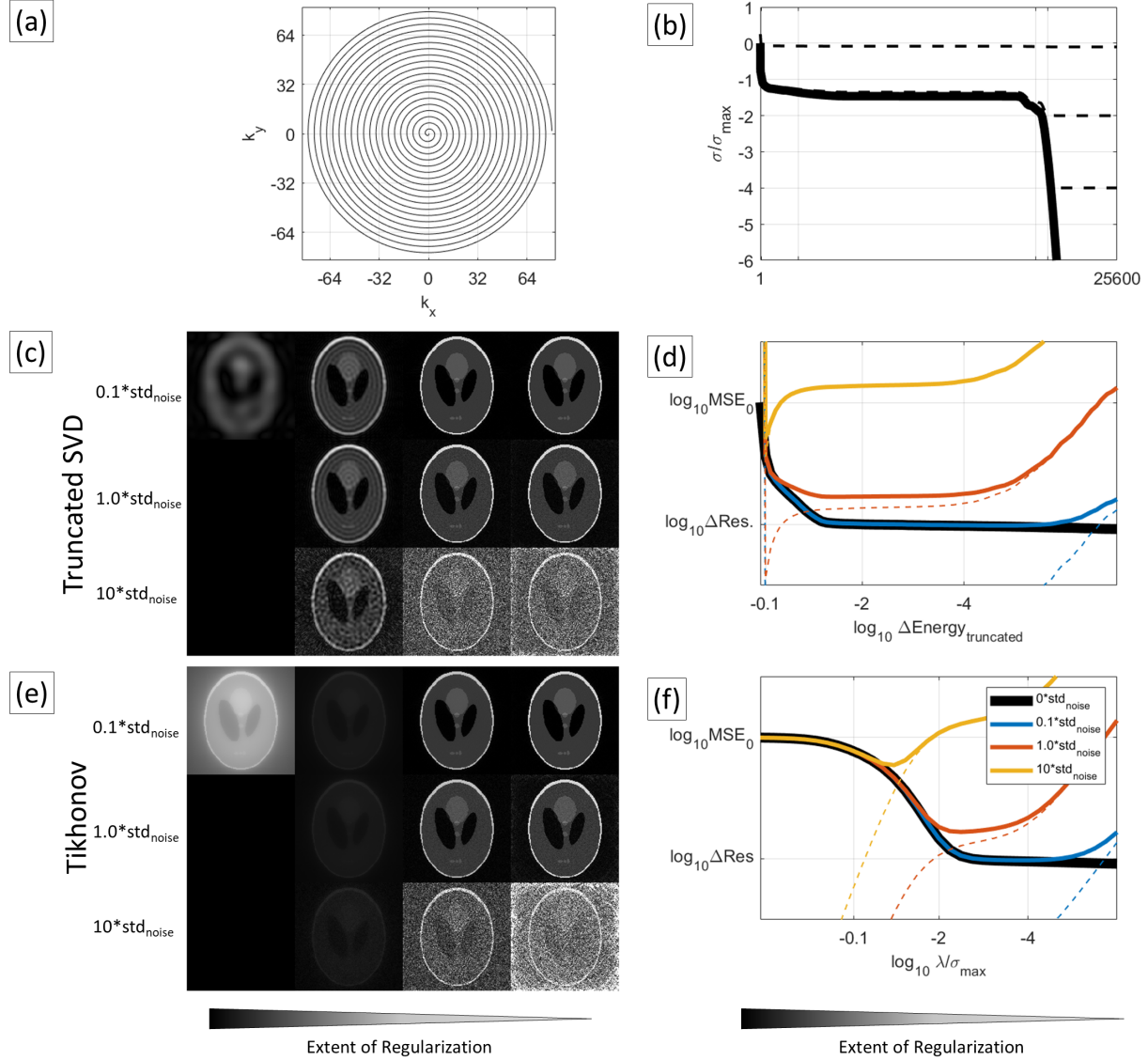


Figure 2: Shepp-Logan Phantom simulations showing the effects of different regularization approaches. (a) The MTX  $128 \times 128$  spiral trajectory used for simulating the forward encoding and inverse reconstruction. (b) The SVD spectrum of the encoding matrix, with vertical lines showing the truncation of the SVD at different values. The square root of the singular values of  $\mathbf{Encode}^H \mathbf{Encode}$  after Tikhonov Regularization at corresponding values are plotted in black dotted lines. (c, e) Shepp-Logan images with different noise levels reconstructed with decreasing regularization from left to right with tSVD and Tikhonov regularization respectively. (d, f) Graphs of MSEs against regularization for varying noise levels, with solid lines showing the MSEs between the original Shepp-Logan image and the reconstructed Shepp-Logan image, and the dotted lines showing the MSEs between purely reconstructing the noise and the ideal Shepp-Logan image. Extent of regularization is expressed for tSVD as the cumulative energy truncated ( $\Delta \text{Energy}_{\text{truncated}}$ ), and for Tikhonov regularization as the regularization parameter divided by the largest eigenvalue ( $\lambda/\sigma_{\max}$ ).

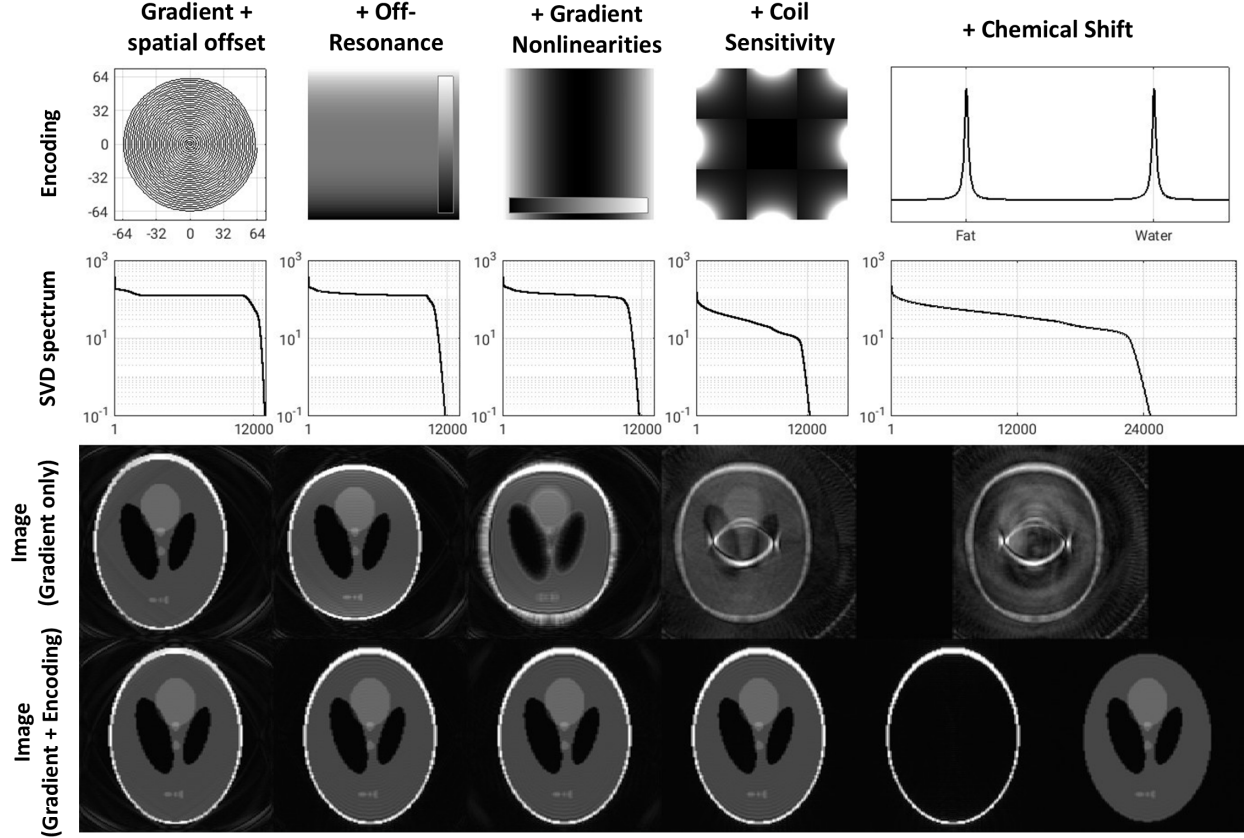


Figure 3: Illustration of additional encoding included in Pinv-Recon as a single unified framework. From top to bottom: encoding mechanism, SVD spectrum of encoding matrix, reconstructed image accounting for gradient encoding only, reconstructed image accounting for gradient and other encoding. From left to right: spiral gradient encoding + spatial off-center positioning, +  $B_0$  off-resonance, + gradient nonlinearities, + coil sensitivity encoding (with 2x2 undersampling of the data), + chemical shift separation (of water and fat).

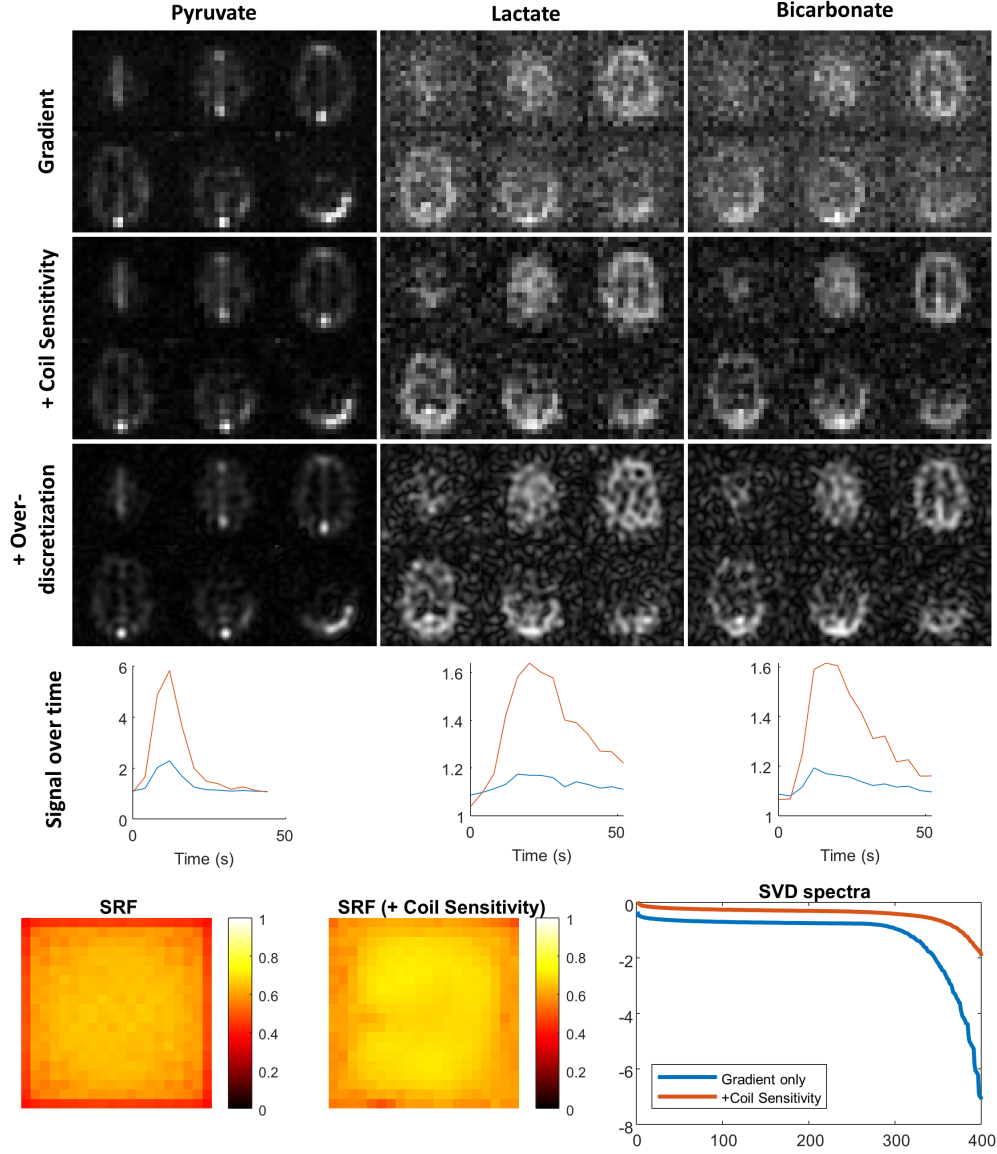


Figure 4: Application of Pinv-Recon on multichannel hyperpolarized carbon-13 data. From left to right: Pyruvate, Lactate, Bicarbonate. From top to bottom: root-sum-of-squares coil combination, Pinv-Recon with coil sensitivity map included, Pinv-Recon with coil sensitivity map included on an overd discretized spatial grid (MTX  $64 \times 64$ ). Only six out of eight acquired slices are shown, as there is little signal in the remaining slices. Mean SNR for the first two methods are plotted in the bottom row in blue and red respectively. The bottom row shows the SRFs and noise maps from the reconstruction with and without coil sensitivity included respectively.

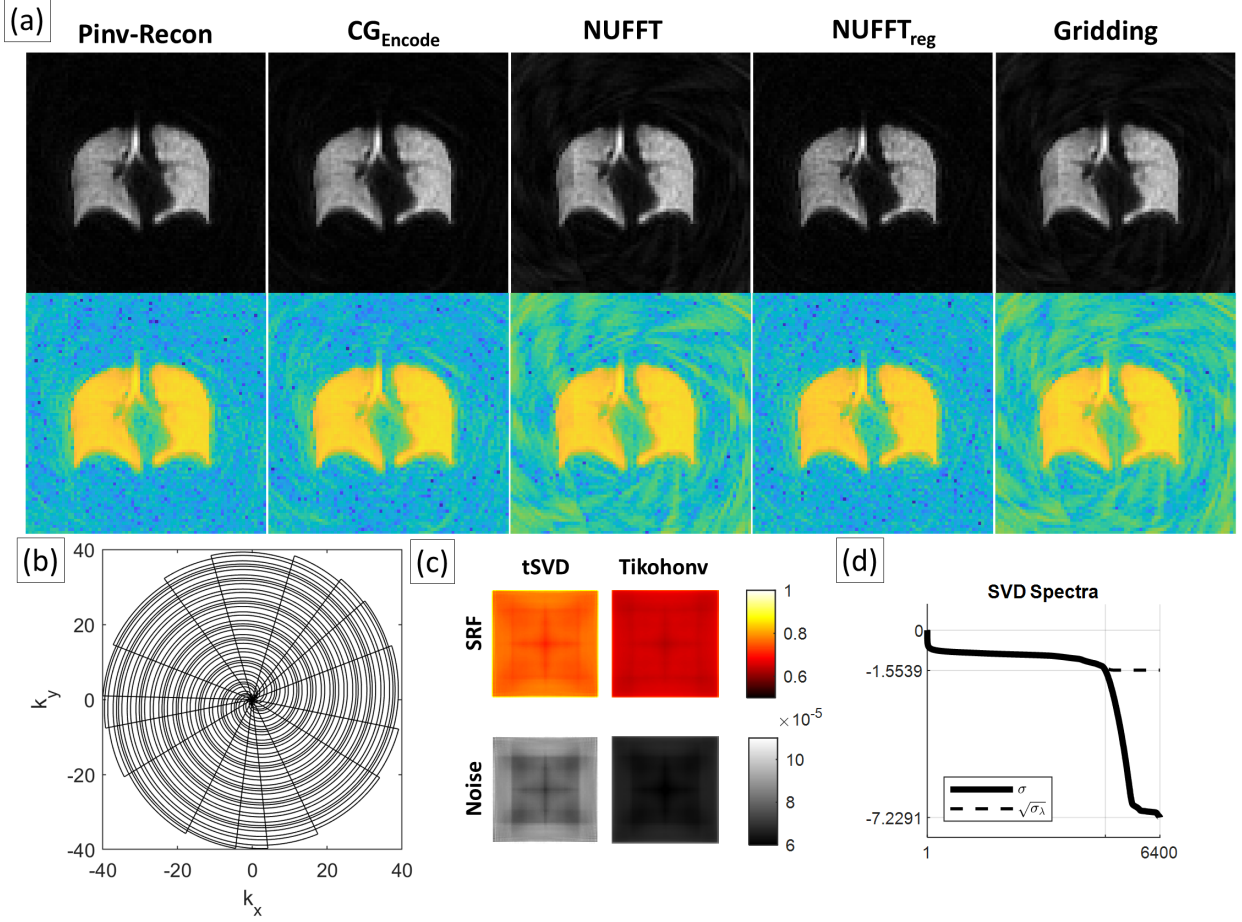


Figure 5: (a) Reconstruction of stack-of-spirals data using, from left to right, Pinv-Recon,  $CG_{Encode}$ , NUFFT, NUFFT with regularization, and gridding. Gridding and NUFFT results in streaking artifacts that can be reduced with regularization, whilst Pinv-Recon eliminates these artifacts and boosts SNR. First row shows the images in the original scale, and second row shows them in log scale. (b) The golden angle spiral in one Z phase-encode of the stack-of-spirals trajectory (c) Top row: the SRFs for tSVD regularization and Tikhonov regularization respectively. Bottom row: the corresponding noise matrices (d) The singular values of **Encode**, with the singular values of the Gram matrix after Tikhonov regularization shown by the dotted line.

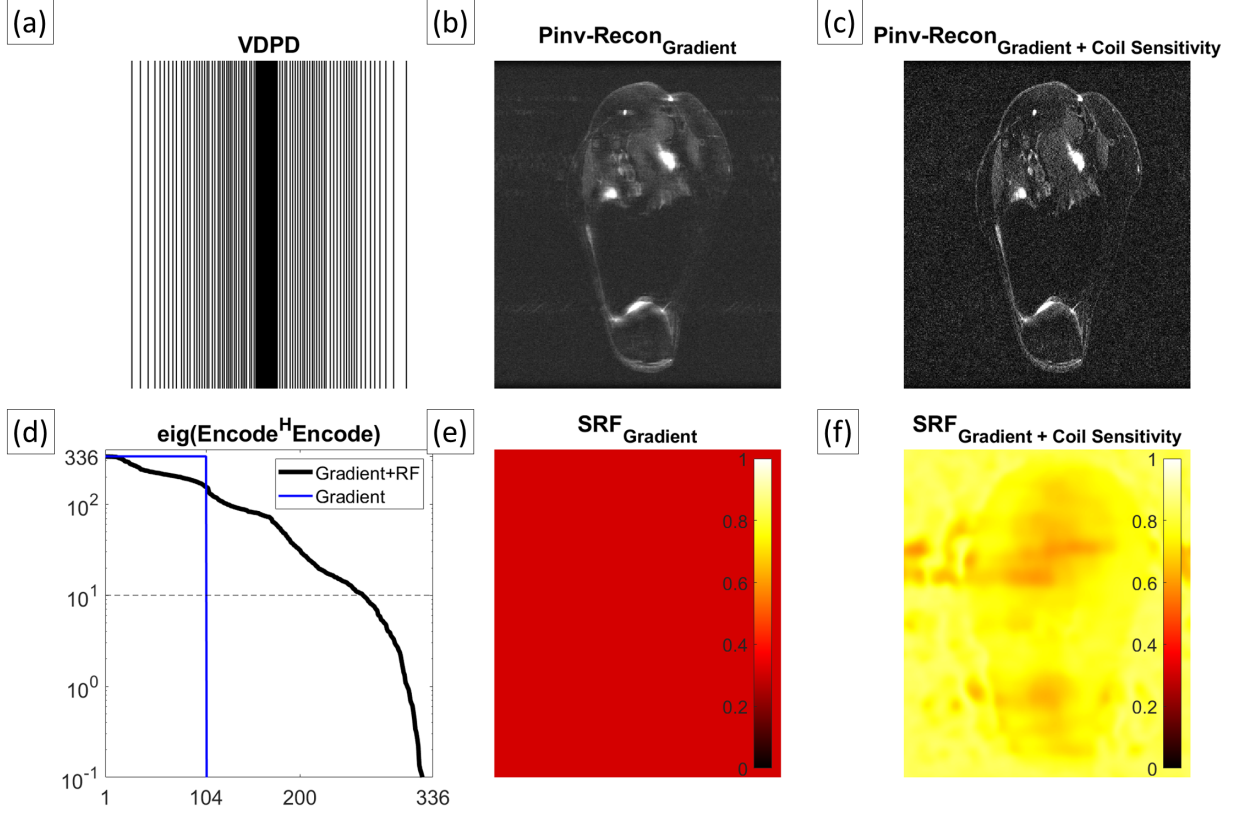


Figure 6: High Resolution  $T_2$ -weighted knee image reconstructed with Pinv-Recon. (a) Plot of the k-space trajectory, showing variable sampling along the phase encoding dimension from left to right (b) Reconstructed image using gradient encoding only (c) Reconstructed image using gradient and coil sensitivity encoding (d) Eigenvalue spectrum, for gradient encoding only (blue) and for gradient encoding with coil sensitivity encoding (black) (e) SRF for reconstruction with gradient encoding only (f) SRF for reconstruction with gradient encoding and coil sensitivity encoding.



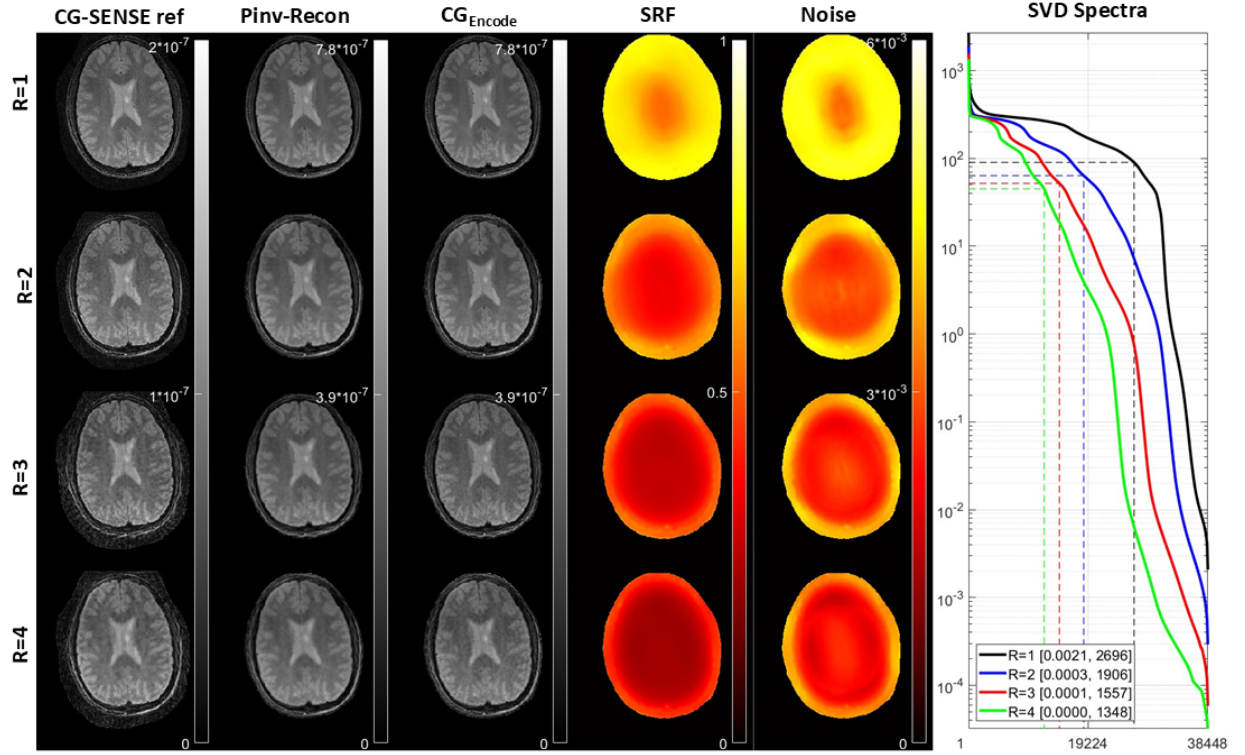


Figure 7: CG-SENSE reproducibility challenge dataset. From top to bottom: undersampling factors from 1 to 4. From left to right: reconstruction using CG-SENSE reference implementation in MATLAB, reconstruction using Pinv-Recon with coil sensitivity encoding, reconstruction using  $CG_{Encode}$ , SRF maps, noise map, SVD spectra.

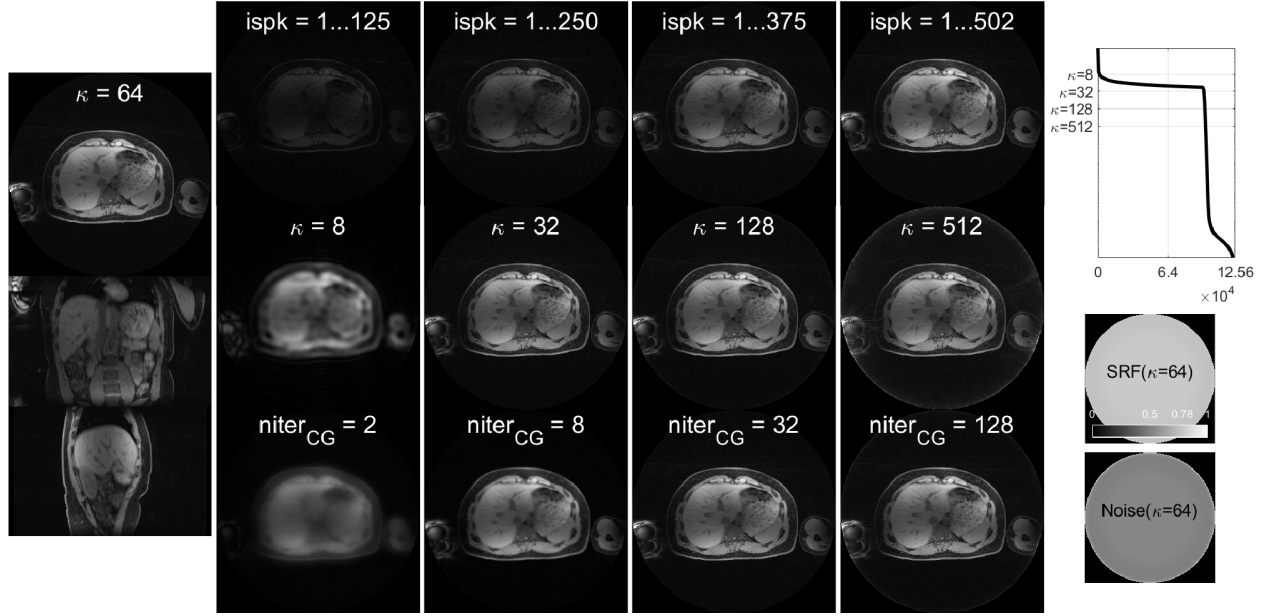


Figure 8: Left: Axial, coronal and sagittal views of the 3D stack-of-stars abdominal imaging dataset. In the middle four columns, top: varying the number of spokes used in reconstruction, middle: varying the condition number  $\kappa$  by changing the tSVD threshold, bottom: varying the number of iterations in  $CG_{Encode}$ . Right: SVD spectrum, SRF map, and noise map.



## Supplementary Materials

### 1 Versatility of Pinv-Recon for Different K-Space Trajectories

Figure S1 demonstrates the versatility of Pinv-Recon for different k-space sampling trajectories, plotting from top to bottom the trajectory, its SVD spectrum, the reconstructed image, the SRF maps, and the Noise matrices. The SVD spectra show that Cartesian sampling is the best-conditioned, as seen also in its artifact-free reconstruction of the Shepp-Logan phantom. Pinv-Recon also allowed the direct calculation of the SRFs of each trajectory, showing all pixels are fully represented in the reconstructed image. The noise matrices reflect that noise is amplified in the edges of the reconstructed image for the radial and spiral trajectories.

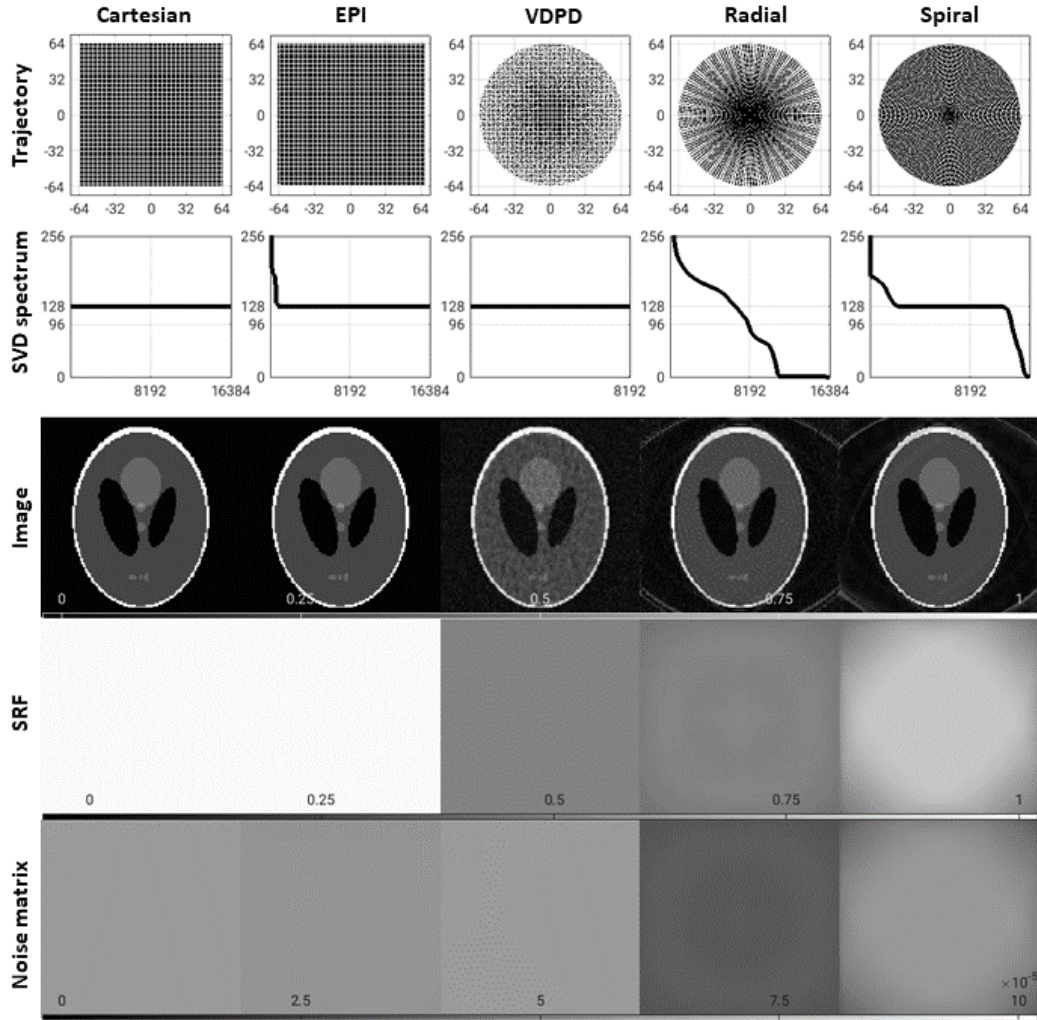


Figure S1: Demonstration of Pinv-Recon on a variety of k-space sampling trajectories. From left to right: Cartesian, EPI, Variable-Density Poisson Disk (VDPD), radial, spiral. From top to bottom: sampling trajectory, SVD, reconstructed Shepp-Logan image, SRF, noise matrix.

## 2 Computational Evaluation on a Mobile Workstation

Section 3.1 listed the computational times required for a high-performance workstation similar to the reconstruction machines found on MRI scanners. Here, we show that even modern mobile workstations with lower-performance can manage the direct pseudoinversion of various encoding matrices. We perform the same computational evaluation described in section 3.1.1 on a Precision 7680 mobile workstation (Dell, Texas, USA), which has 13th Gen Intel® Core™ i9-13950HX, 2200 Mhz, 24 Core(s), 32 Logical Processor(s), 64.0 GB of Installed Physical Memory (RAM), and an NVIDIA® RTX™ 2000 Ada Generation Laptop GPU with 16GB.

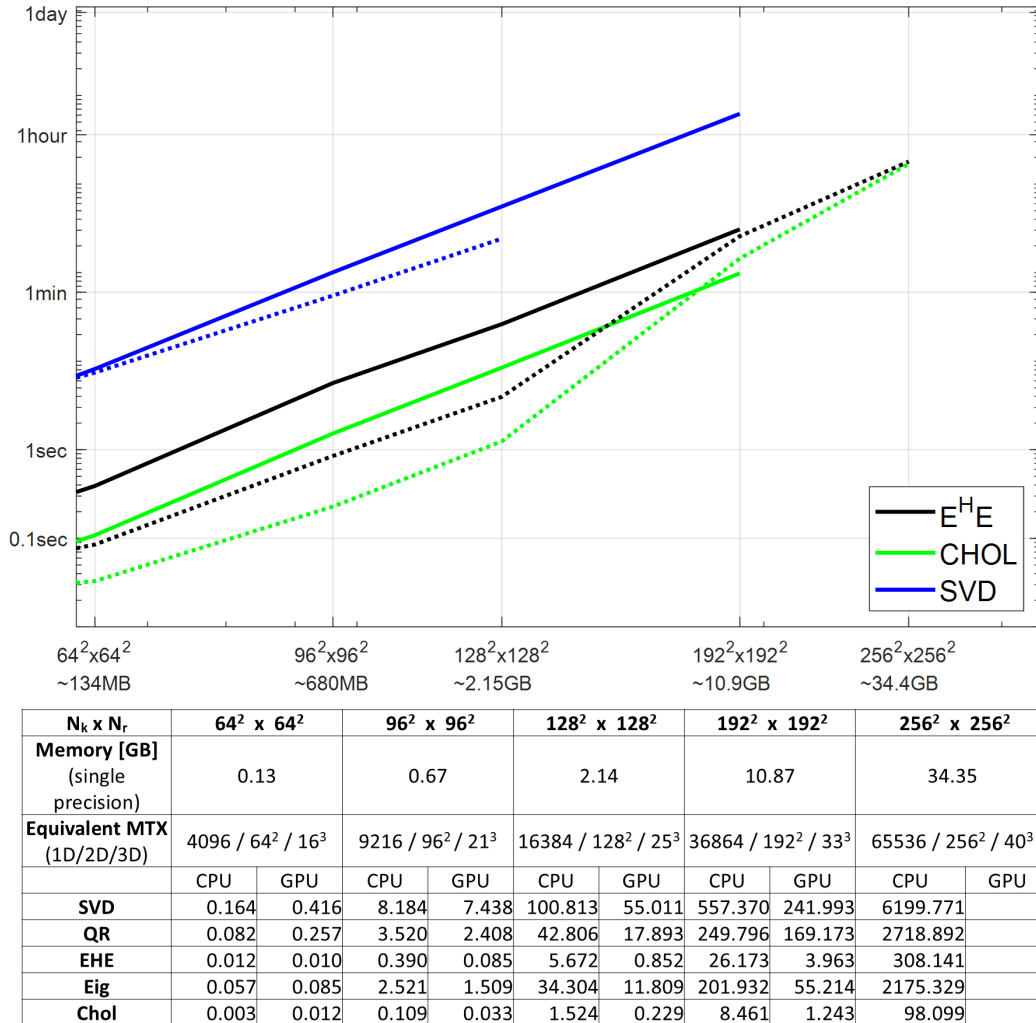


Figure S2: Graph showing computational times for matrix decomposition on a mobile workstation

### 3 $B_0$ Correction Examples

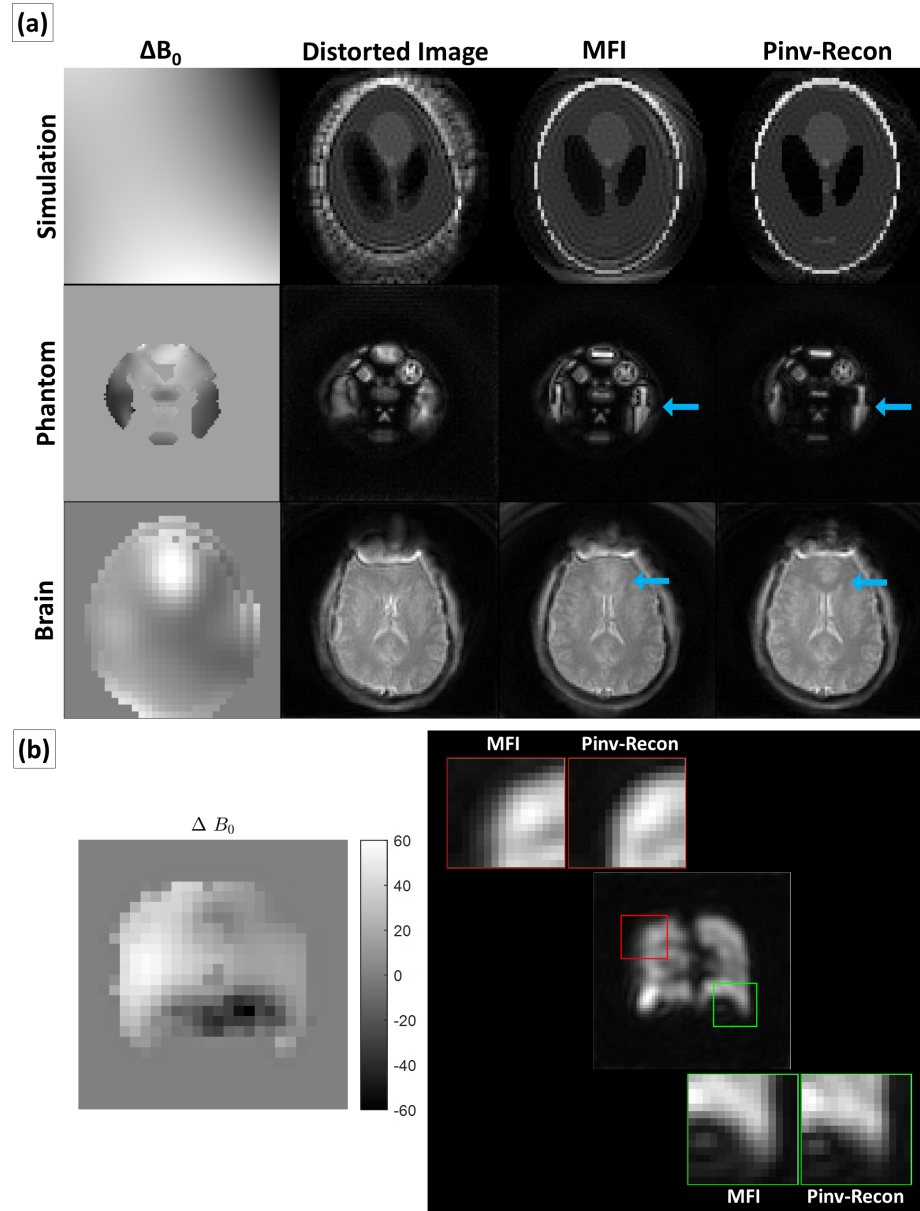


Figure S3: (a) Shepp-Logan simulations, Structural Phantom acquisitions, and in vivo brain acquisitions comparing correction of  $B_0$  distortion using Pinv-Recon versus MFI (b) Left: Off-Resonance Map. Right: Low-resolution hyperpolarized Xenon-129 image, with the original image shown in the center and the  $B_0$  corrected images using MFI and Pinv-Recon shown outside

	MTX 48		MTX 64		MTX 96	
	Pinv-Recon	Gridding	Pinv-Recon	Gridding	Pinv-Recon	Gridding
<b>MSE</b>	0.001343	0.001667	0.000971	0.001736	0.000877	0.002350
<b>PSNR</b>	28.72	27.78	30.12	27.60	30.57	26.29
<b>SSIM</b>	0.8194	0.7859	0.8206	0.7815	0.8465	0.7670

Table 1: Results comparing  $B_0$  correction using Pinv-Recon versus using gridding with MFI correction in a structured resolution phantom.

Figure S3 shows two examples of including  $B_0$  correction in the Pinv-Recon encoding matrix, compared to  $B_0$  with Multifrequency Interpolation (MFI) [6]. Figure S3a shows  $B_0$  correction in a Shepp-Logan simulation, a structured resolution phantom and in vivo a human brain scan at the proton frequency. The off-resonance maps are shown in column 1, the distorted images are shown in column 2. By incorporating the  $B_0$  maps into Pinv-Recon and into an MFI correction for the image obtained through gridding reconstruction, the blurring effects can be ameliorated, recovering images close to the reference image. Pinv-Recon results in lower MSE, higher PSNR, and higher SSIM than MFI for all of the matrix sizes (Table 1).

Figure S3b shows low resolution 2D spiral hyperpolarized Xenon-129 lung dataset, which had a longer readout time. Off-resonance blurring can be observed in the original image. Using gridding reconstruction with MFI correction and using Pinv-Recon with embedded  $B_0$  encoding improved image quality, but Pinv-Recon sharpens the image to a greater extent.

The acquisition details for the proton dataset were maximum gradient amplitude = 30 mT/m; slew rate = 120 T/m/s; FOV = 240×240 mm; bandwidth = 250 kHz. Acquisition parameters: Flip Angle = 30°; TR = minimum TR; Slice thickness = 3mm). The matrix 48 four-arm spiral was repeated at five different TEs ([0,1,2,5,10]ms) to iteratively fit for a  $B_0$  map using the MEDI toolbox. The phantom was imaged in a 3T GE Premier scanner and using a 5-channel flexible AIR coil (GE HealthCare, WI). The healthy volunteer (Male; Age 30) was scanned in the same scanner using a 16-channel receive-only headcoil (GE HealthCare, WI), using the same single-arm MTX96 spiral and the four-arm MTX 48 spiral.

Those for the low-resolution 2D spiral integrated into the Transmit Gain Calibration of a hyperpolarized Xenon-129 scan, which used a 10% dose of Xenon. The participant (Female; Age 24) inhaled 1 L hyperpolarized gas containing a mixture of xenon, polarized for ~10 min, and nitrogen (0.1:0.9 L, respectively). FOV = 400×400 mm, 1.8 ms partially self-refocused excitation pulse, TR = 230 ms, bandwidth = 250 kHz. The  $B_0$  map was determined by repeating this acquisition at echo times of 1.4, 2.3, 3.9, 6.5, 10.8, 18, 30, 50ms then fitting with the MEDI toolbox.

## 4 Arterial Spin Labelling Example

Other suitable applications for Pinv-Recon are medium-resolution functional imaging applications such as Arterial Spin Labelling (ASL). This figure shows an example of reconstructing a stack-of-spirals ASL dataset (MTX  $128^2 \times 42$ , FOV =  $240 \times 240$  mm, 8 arms, TR = 4.8 s, TE = 10 ms).

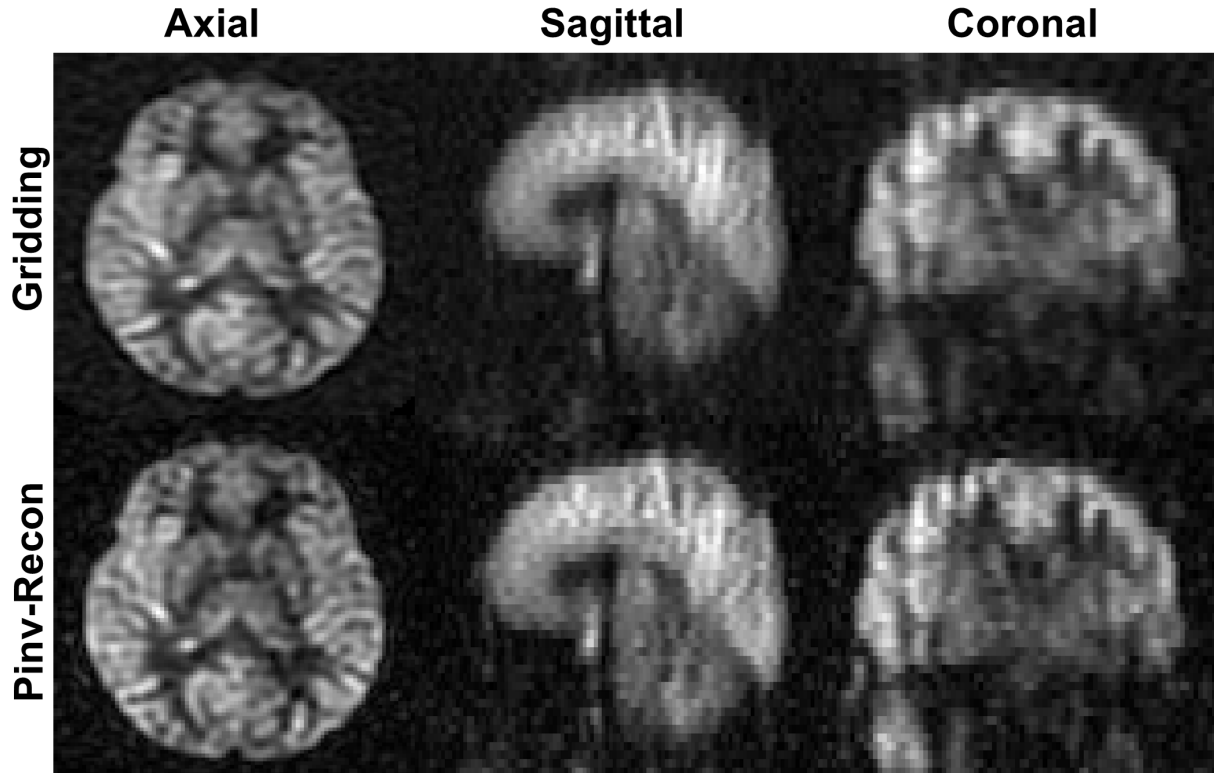


Figure S4: Example of reconstructing ASL data using Gridding Pinv-Recon.